PLANETARY SCIENCE INSTITUTE

PLANETARY SCIENCE INSTITUTE

TABLE OF CONTENTS

TASK 1.1: SPECTROPHOTOMETRIC OBSERVATIONS AND ANALYSIS OF ASTEROIDS

Principal Investigator: Clark R. Chapman

During late 1978 and 1979, major accomplishments were made in the asteroid spectrophotometry program. A chief focus for this research was the international conference on asteroids held at Tucson, Arizona, in spring 1979. Prior to this conference, Chapman (in collaboration with Gaffey) completed the reduction of spectra obtained during 1975 through 1978 at the Kitt Peak, Mauna Kea, and Lowell observatories. A new calibration was employed. Previously published spectra were recalibrated and averaged with new spectra in many cases. The resulting library of visible and near-IR spectra for 277 asteroids was contributed to the TRIAD data file prior to the Tucson conference.

Subsequent to the conference, preliminary work began on interpreting the spectra, including the sorting of spectra into approximately 80 different groups of similar spectra. Work was also done in understanding the fundamental basis for the spectral variety of asteroids. For example, it was demonstrated that the spectra of Eos family asteroids could be synthesized by an appropriate mixture of C and S type materials; the albedos of Eos asteroids are also consistent with the required mixture.

Chapman prepared a summary chapter in the book Asteroids (University of Arizona Press) emanating from the Tucson conference. It concerns the physical nature, interrelations, origin, and evolution of asteroids and contains, in particular, a critical review of what is known about asteroidal mineralogies. Chapman also contributed to another chapter in the book, co-authored by Gradie and Williams, dealing with the properties of Hirayama families; Chapman's contribution related to the spectral traits of family members.

During the past year, further progress was made in measuring the reflectance spectra of unusual asteroids. Fifteen asteroids

were measured using the KPNO 2.1m telescope during a May observing run. In April, ten-micron radiometric measurements were made of 20 asteroids using the KPNO 1.3m telescope; preliminary albedos have been obtained, but further reduction of the data is progressing.

Most of the reduced data and papers emanating from this research have been incorporated in the first three Quarterly Reports; readers are referred to those reports for substantive discussion of the results. We list below the papers and presentations made during the past year based wholly or in part on funding from this contract:

Chapters in Asteroids (ed. T. Gehrels, University of Arizona Press), 1979:

Reflectance Spectra for 277 Asteroids (with M.J. Gaffey); see draft manuscript in Second Quarterly Report, Appendix A.

Asteroids: Nature, Interrelations, Origin, and Evolution; see page proofs in Third Quarterly Report, Appendix A.

Families of Minor Planets (with J. Gradie and J.G. Williams)

Abstracts and Presentations

Recent Asteroid Research (invited review), Bull.A.A.S., 10, 592, 1978 (presented at Pasadena DPS meeting)

Constraints on the Derivation of All Meteorite Classes from the Asteroid Belt, Meteoritics 13, 406-407.

Interpretation of Spectra for 277 Asteroids, Presentation at 42nd Annual Meeting, Meteoritical Society, Heidelberg

Nature and Origin of Minor Planets (invited reivew), European Geophysical Society meeting (Symposium 14 on Evolution of Planetary Bodies), Vienna

Interpretation of Spectral Variety Among the Asteroids, Bull. A.A.S., 11, 562, 1979 (Presented at St. Louis DPS meeting)

TASK 1.2: FURTHER OBSERVATIONS OF PECULIAR ASTEROID 624 HEKTOR

Principal Investigator: William K. Hartmann

Observations of Hektor on four nights (April 3-6, 1979) with the 224 cm telescope at Mauna Kea observatory were successfully obtained. These established lightcurves in both the thermal infrared and reflected sunlight. Comparison of these allowed the first test of whether Hektor's extremely high-amplitude lightcurve is due to elongated shape or albedo patchiness. Analysis showed the lightcurves to be in phase, proving that an elongated shape is the reason for the light variation, fitting the hypothesis published by Hartmann and Cruikshank (1978, Icarus 36, 353-366) developed in previously-funded studies in this program. We reported these results at the St. Louis meeting of the Division of Planetary Sciences of the American Astronomical Society in October 1979.

A manuscript has been submitted to Science, summarizing the work (see Appendix A). Future observations of Trojan asteroids and related objects have been planned with Dr. Cruikshank and Dr. Johan Degewij.

TASK 2: SEARCH FOR FURTHER ASTEROID CLOSE ENCOUNTERS SUITABLE FOR MASS DETERMINATION

Principal Investigator: Donald R. Davis

The goal of this task is to obtain mass estimates for additional asteroids based on close encounters between one of the ten largest asteroids and another numbered asteroid that would produce observable perturbations in the smaller asteroid's orbit. Theoretical analysis of simulated observations determines the best observational strategy as well as the measurement precision necessary to measure the mass of the perturbing asteroid. Observations of perturbations in asteroid orbits resulting from close encounters or near-commensurabilities in the orbital motion have led to mass estimates for three asteroids, namely Ceres, Pallas and Vesta (Hertz, H.G., 1968, Science 160, 299; Schubart, J., 1975, Astron. and Astrophys. 39, 147). However, many other asteroids are now known to be much larger and consequently much more massive than previously believed, so the orbital perturbation technique due to close encounters might be applicable to additional objects.

The first step, to identify suitable close encounters, was carried out earlier in this project, using a Keplerian orbit model for asteroid orbits. The search program uses the given target asteroid orbit as one of the ten largest asteroids and searches a file containing the orbits of all numbered asteroids to determine whether close encounters are possible between the two orbits. If not, the search continues with the next asteroid; if encounters are possible, the program computes the time history of the orbits to see if the closest approach distance is less than the desired criteria. If so, the relevant parameters of the encounter such as encounter speed, closest distance, date, etc., are stored. In this manner, all possible close encounters within a certain period of time are found.

Initial searches were computed using conic orbit elements to propagate the asteroid beyond its epoch date, however subsequent checks indicated this technique could have missed some encounter opportunities, so a refined search using integrated orbits has been carried out. The best encounters found so far are summarized in Table I, which gives the encountering asteroids, the encounter date, closest approach and encounter speed. The final column gives the deflection angle, Θ, adopted as a measure of the perturbation, where

$$\Theta = \pi - 2 \tan^{-1} (1 + rv^2/\mu),$$

with r = minimum encounter distance, v = relative speed of encounter and μ, the gravitational parameter of target asteroid = G · M, is calculated assuming a density of 3 gm/cm^3. Θ is essentially the angle through which the asymptote of the hyperbolic approach trajectory is rotated during the close encounter.

Perturbed orbits resulting from the encounters listed in Table I are being integrated forward in time in order to find the expected residual in right ascension and declination as a function of time. From this information, the optimal observing strategy can be defined. The most useful objects for near term observations are those which have periodic close encounters, an encounter that happened several years ago so that perturbations have had a chance to manifest themselves, or those for which a good encounter is coming up shortly so that a high quality pre-encounter orbit can be obtained. During the past year, astrometric observations of several perturbed asteroids have been obtained by E. Bowell of Lowell Observatory; this program will continue in the forthcoming year. It is also anticipated that plate measurements and initial reductions will begin this year. Hopefully, we can begin to obtain mass information in the not-too-distant future.

TABLE 1. BEST ENCOUNTERS FOR ASTEROID MASS DETERMINATION

A) First Priority

Encountering Asteroid	Date	Closest Approacn (AU)	Relative Speed (km/s)	Deflection Angle (")
		Target Asteroid: 4 Vesta		
486 Cremona	11/6/72	.210	1.69	.245
" "	4/30/80	.083	1.92	.146
1393 Sofala	3/16/81	.045	1.79	.311
1914-70EV	11/15/78	.142	1.50	.123
206 Hersilia	6/9/80	.208	2.45	.056
1449 Virtanen	7/14/81	.248	1.77	.058
1634-1935QP	5/19/84	.113	1.20	.284
2009	7/19/80	.165	1.92	.074
		Target Asteroid: 10 Hygiea		
111 Ate	4/29/78	.102	1.90	.071
1200 Imperatrix	8/22/79	.179	1.65	.054
1482 Sebastiana	6/8/78	.053	2.31	.081
		Target Asteroid: 15 Eunomia		
1284 Latvia	6/13/77	.024	1.53	.104
" "	10/2/81	.039	1.42	.074
		Target Asteroid: 16 Psyche		
1542 Schalen	5/30/82	.245	0.52	.068
1725 Crao	9/16/84	.166	0.26	.403
		Target Asteroid: 65 Cybele		
1778 Alfven	1/31/72	.110	1.06	.069
		Target Asteroid: 704 Interamnia		
881 Athene	9/6/86	.046	1.81	.107

TABLE 1. BEST ENCOUNTERS FOR ASTEROID MASS DETERMINATION (cont.)

B) Second Priority

Encountering Asteroid	Date	Closest Approach (AU)	Relative Speed (km/s)	Deflection Angle (")
	Target Asteroid: 4 Vesta			
126 Velleda	7/9/82	.012	3.87	.245
460 Scandia	12/16/72	.013	3.63	.261
873 Mechthild	7/2/85	.107	1.93	.113
1549 Mikko	8/29/70	.156	2.20	.059
1966	3/6/73	.133	2.23	.068
1516 Henry	2/23/85	.088	2.02	.125
1601 Patry	3/19/88	.066	1.26	.414
1831 Nicholson	5/30/82	.211	1.60	.083
1904 Massevitch	1/20/84	.253	1.79	.055
1914	7/4/83	.112	2.41	.069
	Target Asteroid: 10 Hygiea			
382 Dodona	8/13/73	.131	1.68	.071
1273 Helma	12/22/71	.170	1.70	.054
1135 Cochlis	2/2/89	.061	2.70	.059
	Target Asteroid: 15 Eunomia			
1313 Berna	3/22/70	.039	0.91	.178
	Target Asteroid: 16 Psyche			
1122 Neith	1/25/75	.023	1.94	.052

The search also uncovered some unusual encounters including several very low approach velocity encounters, particularly the 16 Psyche-1725 Crao encounter at 0.26 km/sec which is by far the lowest encounter speed yet found, lower by a factor of $\sim$20 than the mean encounter speed in the asteroid belt. It is interesting to speculate that the mechanism proposed by Hartmann and Cruikshank to explain the irregular shape of Hektor, namely a very low velocity collision between two nearly equal size objects that results in coalescence rather than fragmentation, also operates in the mainbelt and could produce objects such as 15 Eunomia or 45 Eugenia, which are large, irregular-shaped objects.

TASK 3: INFRARED SEARCH FOR INTRA-MERCURIAL BODIES

Principal Investigator: Donald R. Davis

This task consisted of two parts, the first and major portion of the effort is an observational search for bodies hypothesized to orbit interior to Mercury's orbit. This was the first year that observing time was devoted primarily to searching for these bodies, and a report on this year's observing runs is included as Appendix E. The other part of the search for intra-Mercurial objects is a theoretical investigation into the likely location and properties of such objects. Results of this study are summarized in Appendix F.

TASK 4: SEARCH FOR VENUS ASHEN LIGHT

Principal Investigator: William K. Hartmann

The program attempted ground-based detection of emission from the night side of Venus in wavelengths where Soviet spacecraft detected such emissions. Observations were successfully obtained on several dates with the Haleakala solar coronagraph telescope and no emission from Venus was detected. Tables were drawn up to compare low-level emissions from various planetary sources such as the Io cloud) to evaluate the feasibility of further observations. No publication was deemed warranted.

TASK 5: MULTICOLOR AREAL PHOTOMETRY OF URANUS AND NEPTUNE

Principal Investigator: Michael J. Price

In collaboration with Dr. Otto G. Franz (Lowell Observatory), we extended our investigation of structure on the Uranus disk, and began a similar investigation of Neptune. Our results are repeated in two papers, submitted for publication in Icarus. We reported our results at the 1979 AAS/DPS Meeting in St. Louis.

In collaboration with Dr. Michael J.S. Belton (Kitt Peak National Observatory), we investigated the rotation period of Neptune, making use of our recent observational data. A third paper was submitted for publication in Icarus. All these papers are reproduced in Appendices B, C, and D.

Papers

1. Uranus: Disk Structure within the 7300 Angstrom Methane Band, Icarus 39, 459-472, 1979.

2. Neptune: Limb-Brightening Within the 7300 Angstrom Methane Band (in review).

3. Neptune's Rotation Period: A Correction and A Speculation on the Effect of the Disk Brightness Distribution (in review).

TASK 6: GROUND-BASED OBSERVATIONS OF THE GALILEAN SATELLITES TO SUPPORT THE VOYAGER MISSION

Principal Investigator: Kevin Pang

Analysis of two-beam multispectral photometer observations of the Galilean satellites taken on the night of December 28, 1978, using the 224-cm telescope on Mauna Kea is partially complete. Figure 1 shows the relative spectral reflectance of Ganymede between 0.23 and 0.95 μm (normalized to 1.0 at 0.56 μm). The reflectance spectrum was published in the August 30th issue of Nature 279, 805 (1979). It also serves as the ground-truth reference to compare Voyager 2 multispectral photometric (PPS) observations of the Galilean satellites' width. There is generally good agreement between our ground-based data (squares) and Voyager data (triangles). The 725-nm Voyager PPS data point was found to be consistently higher than neighboring ground-based data. The cause of this discrepancy is being looked into.

The ultraviolet reflectivity of Ganymede, as observed by Voyager 2 PPS, was found to agree well with that observed by OAO-2 (diamonds) (Caldwell, 1975). Both data sets show a monotonic decrease with decreasing wavelength. This behavior does not agree with upturns in geometric albedo reported by ground-based observers (triangles and circles in Figure 2) (Johnson and McCord, 1971; Wamsteker, 1973, respectively). High resolution ground-based observations by Nelson and Hapke (1978) does not show this upturn either (continuous curve in Figure 2). The same upturn was also seen in our own observations (squares in Figure 2). The P.I. discussed this discrepancy with Lucy McFadden (McCord's group) and Bob Nelson. Ms. McFadden feels that this was due to a calibration problem. When she calibrated Johnson's observations by referencing to a different

star, the resulting μv reflectance decreases monotonically with decreasing wavelength also. Therefore, it appears that all observers, with the possible exceptions of Wamsteker (who is no longer active in this field) now agree that the upturn in Ganymede's reflectance spectrum is spurious. The P.I. supplied the Voyager data set to Ms. McFadden. It is expected that a summary of visible reflectance data on the Galilean satellites will be published soon (McFadden et al., to be submitted to Icarus, 1979).

REFERENCES

Caldwell, J. (1975). Ultraviolet Observations of Small Bodies in the Solar System by OAO-2. Icarus 25, 384-396.

Johnson, T.V., and McCord, T.B. (1971). Spectral Geometric Albedo of the Galilean Satellites, 0.3-2.5 microns. Astrophys. J. 169, 569-593.

McFadden, L.A., Bell, J., and McCord, T.B. (1979). Visible Spectral Reflectance Measurements 0.3-1.1 μm of the Galilean Satellites at Many Orbital Phase Angles 1977-1978. To be submitted to Icarus.

Nelson, R.M., and Hapke, B. (1978). Spectral Reflectivities of the Galilean Satellites and Titan, 0.32-0.86 Micrometers. Icarus 36, 304-329.

Wamsteker, W. (1972). Narrow-Band Photometry of the Galilean Satellites. Comm. Lunar Planet. Lab. 9, 171-177.

FIGURE 1

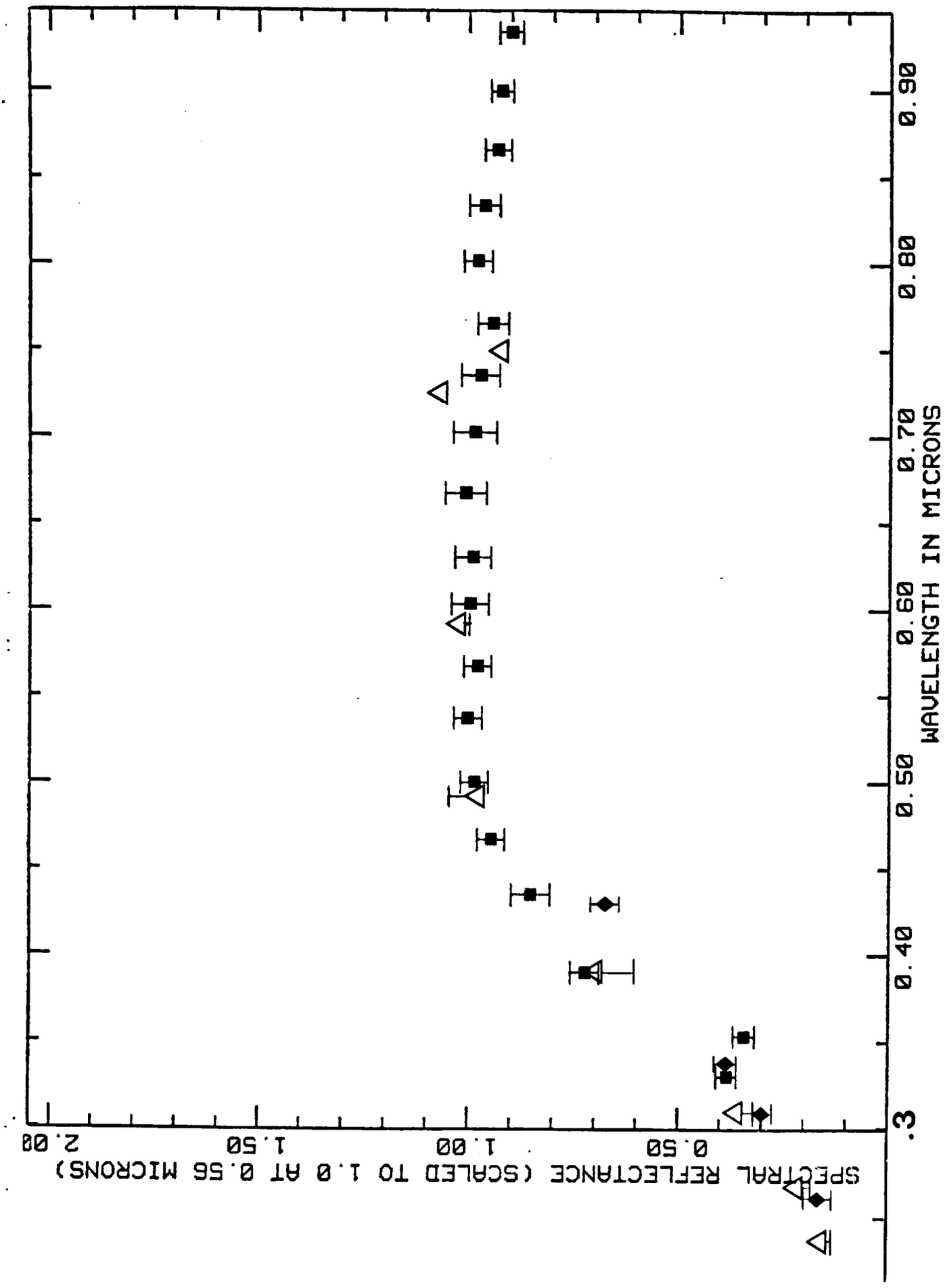
SPECTRAL REFLECTANCE (SCALED TO 1.0 AT 0.55 MICRONS)
0.50
1.00
1.50
2.00
.3
0.40
0.50
0.60
0.70
0.80
0.90
WAVELENGTH IN MICRONS

FIGURE 2

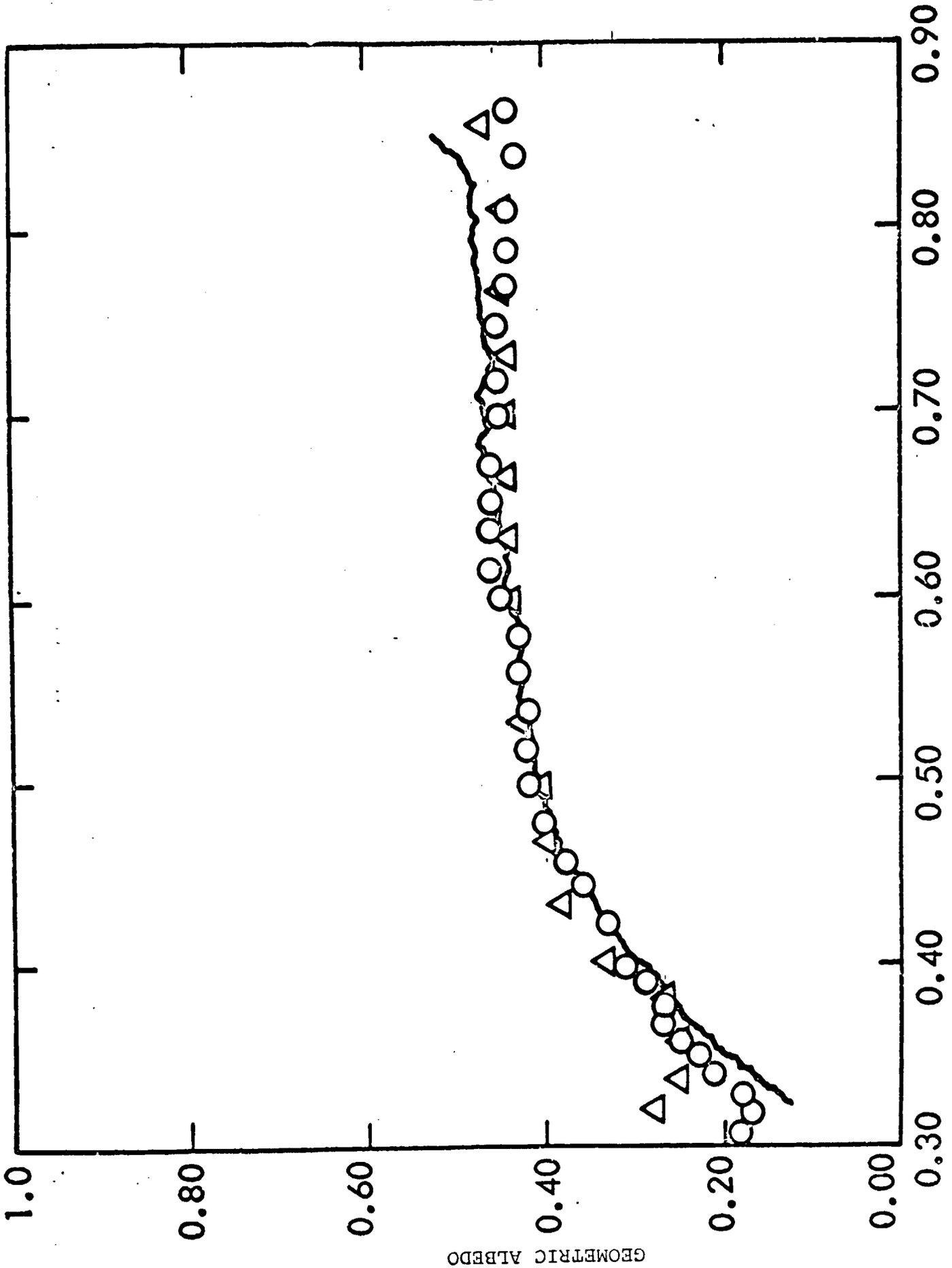
GEOMETRIC ALBEDO
1.0
0.80
0.60
0.40
0.20
0.00
0.30
0.40
0.50
0.60
0.70
0.80
0.90
WAVELENGTH MICROMETERS

APPENDIX A

HEKTOR: THE LARGEST HIGHLY ELONGATED ASTEROID

by

William K. Hartmann
Planetary Science Institute
2030 East Speedway
Tucson, Arizona 85719

and

Dale P. Cruikshank
Institute for Astronomy
University of Hawaii
Honolulu, Hawaii 96822

Submitted November 12, 1979, to Science

ABSTRACT

New observations of Trojan asteroid 624 Hektor, in April, 1979, establish that the high amplitude of the rotational light curve of this object is caused by elongated shape and not by dark and light albedo patches on opposing hemispheres. These observations confirm that Hektor is a very unusual object, consistent with our earlier hypothesis that it may be a compound asteroid formed when two comparable-sized Trojans fell together - a rare fossilized example of a planetary accretion process.

The trojan asteroids are two groups of minor planets trapped in the Lagrangian points 60° ahead of and behind Jupiter, in Jupiter's orbit. Dunlap and Gehrels (1) discovered that 624 Hektor, the brightest Trojan, has one of the largest amplitudes found among asteroid light curves. The brightness can change by as much as a factor of 3.1 during Hektor's 6.9 hour rotation. The amplitude depends upon the geometry of observation, since Hektor's rotation pole lies near the ecliptic. Dunlap and Gehrels inferred that the light curve amplitude is likely due to a very elongated shape, but had no proof that the variations were not due to albedo markings. Cruikshank (2) and we (3) established that the two polar faces of Hektor have very low average albedo so that Hektor is much larger than had first been thought. Currently estimated dimensions are about 150 x 300 km. Degewij (4) found that other Trojans have light curve amplitudes typically only 10 to 20% and are evidently roughly spheroidal.

As reviewed in more detail by us (3), these observations make Hektor a very puzzling object. The conventional explanation for an elongated asteroid is that it is a splinter-shaped fragment of a larger body, but in Hektor's case, this would require one huge splinter-shaped fragment with a swarm of smaller spheroidal fragments, all trapped in the same

cloud, and therefore, presumably originating from some unknown still-larger parent Trojan, with no obvious cause for fragmentation. This scenario seems ad hoc and unappealing. The other alternative would be that Hektor is a spheroidal object with one dark and one light hemisphere like Saturn's satellite, Iapetus. This would also be extraordinary, however, since Hektor has no obvious preferred orientation in space, while the Iapetus albedo variations are correlated with the leading and trailing hemispheres, and believed associated with a sweep-up of debris as Iapetus moves in its orbit, keeping one face tidally locked toward Saturn.

Furthermore, most of the known highly elongated asteroids are among the smallest known asteroids only a few kilometers in length. They make plausible fragments. However, among the thousands of asteroids, Hektor ranks about the 21st in dimension and has the third highest amplitude light curve!

We (3) attempted an explanation of these properties with a more physical model than had been suggested earlier, namely, that Hektor had formed during a relatively low velocity collision of two earlier spheroidal Trojans, which had insufficient energy to completely fragment each other and thus formed a partially fragmented, compound asteroid with an elongated or dumbbell-like shape. The collision might have either been the product of inward spiralling during tidal evolution of a co-orbiting pair (very low speed), or a random low-speed

collision of two neighboring objects in the Trojan cloud. The tidal idea requires an explanation for the initial co-orbiting pair, while the collision of two field asteroids appears to require a somewhat lower approach velocity than would be typical for Trojan asteroids (5). Nonetheless, this model of Hektor's formation through collision is the only published physical hypothesis for Hektor's origin and offers the possibility of an actual example of the coalescence of two primitive planetesimals - the process widely hypothesized to be responsible for the formation of planets. Hektor could thus be not only an interesting but an important object in understanding the history of the solar system.

A nagging problem throughout all this work, was lack of proof that Hektor actually is elongated. We have performed a test of whether Hektor is elongated by obtaining near-simultaneous lightcurves in reflected sunlight and thermal infrared. This discriminates a light curve caused by shape from a light curve caused by albedo patchiness as follows: If the light curve is caused primarily by shape, then both light curves would show simultaneous maxima when the broad side of Hektor faces the observer. However, if the light curve were due to albedo patches, then the maximum in reflected sunlight would correspond to the bright or cooler side, which would produce a minimum in the thermal infrared curve. Therefore, the two light curves would be

correlated in phase if due to elongated shape, but anti-correlated if due primarily to albedo patches.

The amplitudes would also be different in the two cases. If due to elongated shape, the amplitude would measure essentially the cross-section area exposed (modulated by any minor albedo patchiness). But if an albedo effect dominates in producing the reflected light amplitude, then the amplitude of the indrared light curve would depend on temperature difference between the markins and this in turn would depend on the absolute range of albedos. In the case of Hektor, this must be very small since the average albedo of Hektor is about 2 to 3% (2,3). If we assume the albedos of the two hemispheres, with a ratio of 3.1, to approximately 0.012 and 0.038, then that light absorbed by the different regions of Hektor varies between .96 and .99, producing a thermal light curve amplitude of only about 1.02:1. (Alternatively, had Hektor been highly reflective, e.g., with albedo 0.86 on one side and .28 on the other, the thermal light curve amplitude could exceed 5:1.

On April 3-6, 1979, we obtained new light curves with the 224 cm telescope at Mauna Kea Observatory, when Hektor's brightness was varying by about a factor of 2. The reflected sunlight was represented by photometry at 1.2 μm, and the thermal infrared radiation was represented by photometry at

effective wavelength of 20 μm. Using the known rotation period (1), we combined the photometric data from the four nights into a single rotational lightcurve, shown in Figure 1.

Figure 1 establishes that the maxima and minima of the two light curves are correlated, not anti-correlated, and have the same amplitude within the limits of measurement. This establishes in turn that 624 Hektor must have an elongated shape, which accounts for most of the light variation.

In hypothesizing our model for Hektor (3), we pointed out that a compound asteroid consisting of two uniform spheres could not have a light curve amplitude greater than 2:1. Indeed, the original model by Dunlap and Gehrels (1) called for a more elongated, cigar-shaped object to explain the observed light curve, which can reach amplitude 3.1:1 when Hektor is viewed in its equatorial plain. Therefore, we proposed that the crushed material in the contact zone between the two components may be brighter material, analogous to rays around fresh lunar craters. Because of the weakness of the albedo influence on photometry, this "ray" material would be difficult to detect by photometry alone, but might be spectrophotometrically apparent. At any rate, the material exposed in the side view may be different from that seen in the end views. Further, if Hektor formed from two distinct asteroids, the material seen in the two end views (views of the two original objects) may be different from each other.

Since our new results confirm the peculiarity of Hektor's shape and are consistent with the above hypothesis, it is important to follow up with further spectrophotometric observations that might confirm such predicted composition differences. The question of Hektor's origin is puzzling and unresolved, but Hektor may display a fossilized example of the primitive collisional accretion process in action. In any case, we have established that Hektor is the most elongated object of its size and that it is a worthy candidate for future study or possible space craft exploration.

REFERENCES

1. J.L. Dunlap and T. Gehrels, Astron. J. 74, 797-803 (1969).

2. D.P. Cruikshank, Icarus 30, 224-230 (1977).

3. W.K. Hartmann and D.P. Cruikshank, Icarus 36, 353-366 (1978).

4. J. Degewij, Proc. 8th Lunar Sci. Conf. 1, 145 (1977). Ph.D. dissertation, Leiden University (1978).

5. W.K. Hartmann, Asteroids (University of Arizona Press, Tucson, 1979), in press.

6. This work was supported by NASA's Planetary Astronomy program. This is Planetary Science Institute Contribution No. 135.

FIGURE 1: Comparison of simultaneous lightcurves of Trojan asteroid 624 Hektor in reflected sunlight (1.2 μm) and thermal radiation (20 μm). Consistent phase and amplitude of the curves shows that Hektor's light variations are due to an unusually elongated shape, not albedo patchiness.

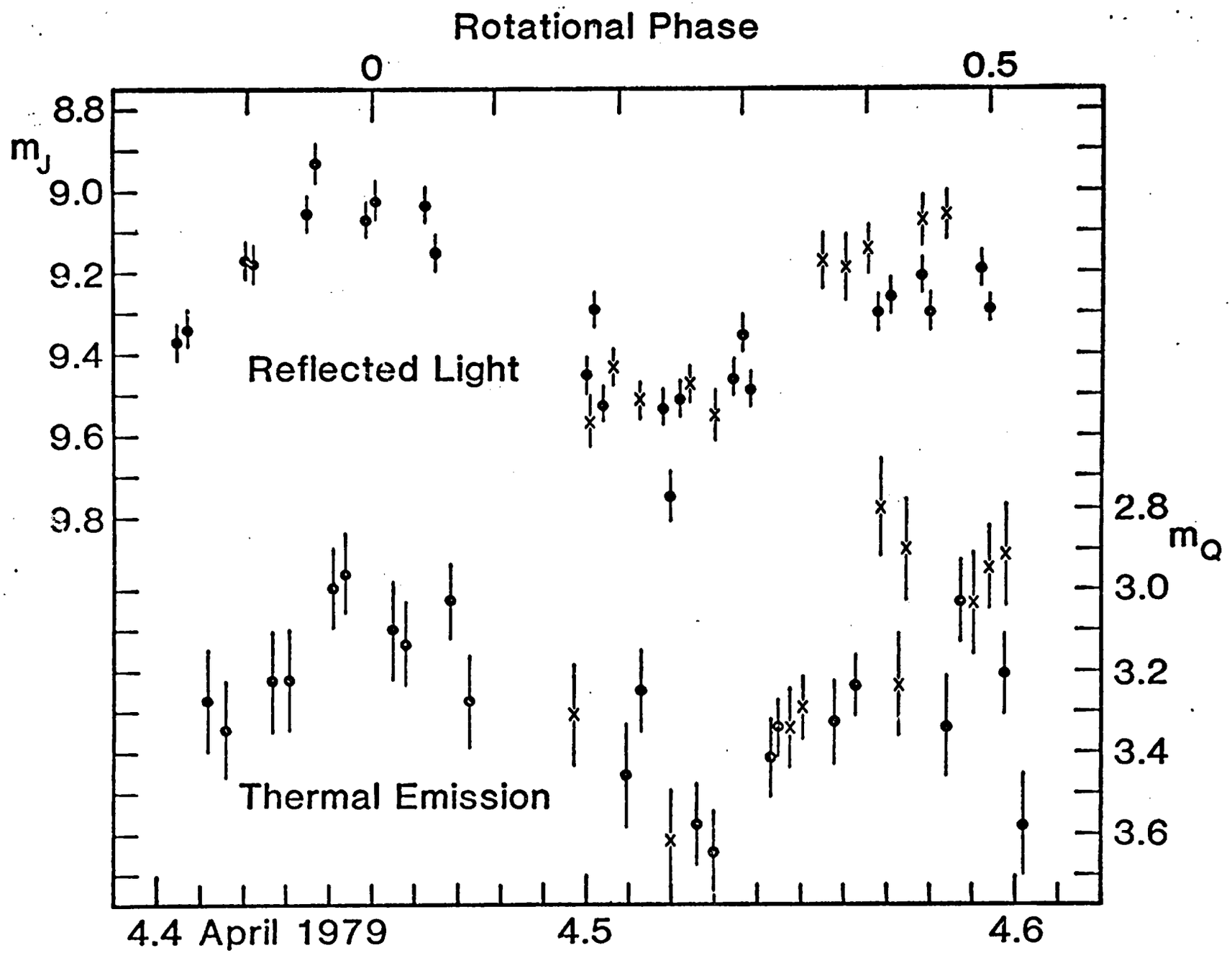
Rotational Phase
0
0.5
8.8
m_J
9.0
9.2
9.4
9.6
9.8
Reflected Light
Thermal Emission
2.8
m_Q
3.0
3.2
3.4
3.6
4.4 April 1979
4.5
4.6

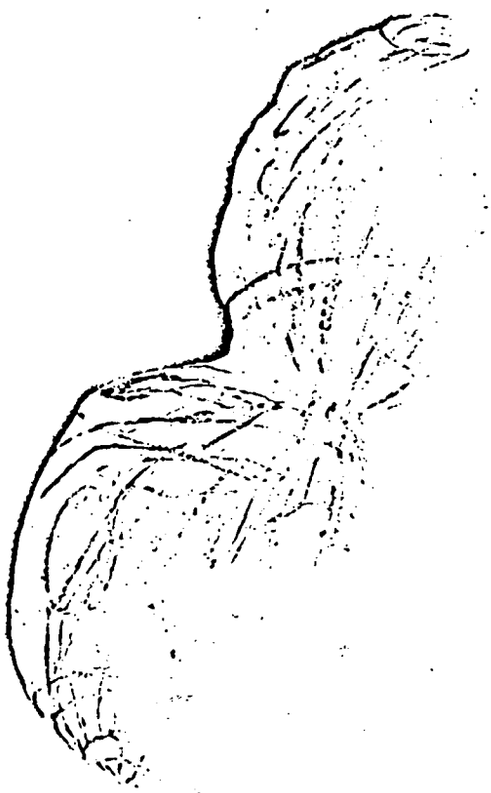

Possible recon. of

REVISED MANUSCRIPT

APPENDIX B

URANUS: DISK STRUCTURE WITHIN THE 7300 ANGSTROM METHANE BAND

Michael J. Price
Science Applications, Inc.
5055 E. Broadway, Suite A-214
Tucson, Arizona 85711

and

Otto G. Franz
Lowell Observatory
P.O. Box 1269
Flagstaff, Arizona 86002

No. of Copies: 3
No. of MS Pages: 21
No. of Figures: 6
No. of Tables: 1

ABSTRACT

Orthogonal narrow-band (100Å) photoelectric slit scan photometry of Uranus has been used to infer the basic two-dimensional structure of the disk within the 7300Å methane band. Numerical image reconstruction and restoration techniques have been applied to quantitatively estimate the degrees of polar and limb brightening on the planet. Through partial removal of atmospheric smearing, an effective spatial resolution of approximately 0.9 arc. sec. has been achieved. Peak polar, limb, and central intensities on the disk are in the respective proportions 3:2:1. In addition, the bright polar feature is displaced from the geometric pole towards the equator of the planet.

1. INTRODUCTION

Although investigations of structure on the disk of Uranus present severe observational problems for ground-based astronomy, both limb and polar brightening have been detected within several deep CH_4 bands. Brief studies of these phenomena have been carried out by Westphal (1972), Sinton (1972) and Smith (1977) at 8900Å, by Franz and Price (1977) at 7300Å, and by Avis et al. (1977) at 6190Å. Continuum polar brightening at 7500Å was also detected by Franz and Price (1977). These studies have indicated the presence of aerosol particles in the upper regions of the Uranus atmosphere.

More extensive investigations were carried out by Price and Franz (1976, 1978). Their observations were concentrated on the two strong CH_4 bands at 6190Å and 7300Å. Coarse quantitative estimates of the true intensity distribution over the Uranus disk were obtained from direct predictions based on arbitrary theoretical models smeared by known atmospheric and instrumental effects. For the 6190Å band, the planet was found to exhibit a disk of nearly uniform intensity. For the 7300Å band, moderate limb brightening was apparent. Specifically, the true intensities at the center and limb of the planetary disk were approximately in the proportion 1:2. Extreme limb-brightening, with a corresponding intensity ratio greater than 1:4, was not permitted. Disk structure was apparent through lack of circular symmetry in the intensity distribution over the Uranus image. Continuum polar brightening at 7500Å was especially prominent. Disk profiles for the 7300Å CH_4 band were used by Price (1978) to derive a lower limit to the CH_4/H_2 mixing ratio in the atmosphere below the aerosol haze. Compared with the solar value, methane appeared to be overabundant by a factor of three or greater. The optical thickness of the aerosol region was estimated to lie in the range 0.1-0.2.

Improved narrow-band (100Å) photoelectric slit scan photometry of Uranus, in the spectral region 6000-8500Å, was carried out by Price and Franz (1979). In each waveband of interest, the disk profile was obtained directly from the photometric data by an image restoration technique. Measurements of the point spread function were used to partially remove the

effects of atmospheric seeing by analytical Fourier-Bessel inversion. Both limb and polar brightening were confirmed to be present within the 7300Å CH_4 band. In addition, weak polar brightening may be present at 6190Å. Surprisingly, however, not all strong CH_4 bands were found to exhibit limb brightening. Specifically, the CH_4 bands at 8000Å and 8500Å showed pronounced apparent limb darkening. Either polar haze in the upper atmosphere or the visibility of a deep dense cloud layer could be responsible for the effect.

Three major simplifications were employed in the Price and Franz (1979) restoration technique. First, the image of the planet was treated as circularly symmetric. Second, its radial intensity distribution was assumed to be precisely defined by the difference between two Gaussian profiles. Third, amplification of the highest spatial frequencies was only loosely controlled by untruncated Gaussian filtering. In this paper, we further develop the restoration technique to permit the investigation of structure on the Uranus disk. New narrow-band (100Å) slit scan photometry of the planet within the 7300Å CH_4 band is reported. Orthogonal scans were obtained to investigate departures from circular symmetry in the Uranus image. Numerical Fourier inversion techniques were used to handle more general distributions of intensity across the planetary disk. Non-physical amplification of the high spatial frequencies during numerical processing of the data was tightly controlled by standard methods of digital filtering. Our quantitative restoration of the Uranus image shows the magnitude of polar and limb brightening on the planet.

2. OBSERVATIONAL DATA

During the 1978 Uranus apparition, narrow-band (100Å) slit scan photometry of the planet within the 7300Å CH_4 band was carried out by the technique described by Price and Franz (1979). On 1978 June 25, excellent observational data were obtained from the area-scanner mounted on the 1.8-meter Perkins reflector at Lowell Observatory. Point spread function (PSF) data were obtained by scanning a star adjacent to the planet. Direct and reverse scans were made along two orientations, south-north (S-N) and east-west (E-W). Samples were taken at spatial intervals of 0".032 arc with a slit of 100μm (0".645 arc) width. Both slit and scan length were 2mm (12".9 arc).

Each recorded scan of Uranus and of the star was obtained by integrating 10 one-second sweeps. This short integration time was chosen to minimize image-wander produced by telescope tracking errors and by variations in the atmospheric refraction. Further shortening of the integration time would have adversely affected the signal-to-noise ratio. To increase the effective signal-to-noise ratio, composites of the integrated scans were subsequently computed, by the method described by Price and Franz (1979). Where necessary, scans made in opposite directions were mirrored on their centroids prior to summation within the computer. For Uranus, the S-N and E-W composites showed significant differences. But no such differences were found for the star. Circular symmetry was therefore assumed for the point spread function. The final stellar composite (Figure 1) was formed by summing the S-N and E-W data. The composite Uranus slit scans, in both directions, are plotted separately in Figure 2. To expedite comparison, both scans have been normalized to equal integrated signals. Total scan numbers of both the stellar and Uranus composites are shown in Table I.

Atmospheric turbulence, together with diffuse instrumental scattering, is responsible for the observed point spread function. Our earlier investigations (Price and Franz: 1978, 1979) showed that the point spread function is well represented by the summation of two colocated but distinct

Table I

FORMATION OF COMPOSITE STELLAR AND URANUS PROFILES AT 7300 ANSTROMS

Scan Object	No. of Integrated Scans	No. of One-Second Sweeps
Star	48	480
Uranus (S-N)	37	370
Uranus (E-W)	38	380

Gaussian curves. Normalizing the point spread function, f(r), to unit total energy, we can write its radial distribution in the form

$$f(r) = \frac{1}{\pi\left[A_p\sigma_{1p}^{\,2} + B_p\sigma_{2p}^{\,2}\right]}\left\{A_p \cdot \exp\left[-r^2/\sigma_{1p}^{\,2}\right] + B_p \cdot \exp\left[-r^2/\sigma_{2p}^{\,2}\right]\right\} \quad (1)$$

where A_p, B_p, σ_{1p} and σ_{2p} are constants. The optimum set of PSF parameters was obtained from the composite stellar slit scan by the method described by Price and Franz (1979). Specifically, we found $A_p = 1$, $B_p = 0.18622$, $\sigma_{1p} = 0\overset{''}{.}816$, and $\sigma_{2p} = 1\overset{''}{.}611$. Our best-fitting theoretical scan is compared with the observational data in Figure 1. Scaled with respect to the central intensity, the root mean square deviation between theory and observation is 0.37 percent. Evidently, the goodness-of-fit is limited by the residual noise in the photometric data. Stability of the point spread function during the course of the observations was high, with extreme fluctuations in its Gaussian 1/e width remaining within $\pm$ 4.4 percent of the mean. The corresponding uncertainty in the basic shape of the point spread function would have a negligible effect on the derived Uranus profiles (Price and Franz, 1978).

3. IMAGE RECONSTRUCTION

Two-dimensional reconstruction of the Uranus image is required prior to restoration. In theory, reconstructing an unknown image from its projections is not difficult. Mersereau and Oppenheim (1974) have reviewed the mathematical procedures involved. But, in practice, reliable reconstruction requires multiple projections of high photometric accuracy spaced closely in position angle. For Uranus, we have only orthogonal slit scan photometry. Even so, reconstruction of the image can be achieved if the limited a priori knowledge of the intensity distribution over the disk of the planet is used.

Within the 7300Å CH_4 band, significant polar and limb brightening are present on the Uranus disk. Detailed examination of pinhole scans of the planet, obtained by Price and Franz (1978), suggests that the true extent of the polar feature is negligible compared with the smear introduced by atmospheric seeing. We can describe the Uranus image by an elementary two component model. Circularly symmetric limb brightening can be represented by an arbitrary radial distribution of intensity. Polar brightening can be described by the point spread function off-set from the disk center. Division of the total energy contained within the Uranus image between the polar feature and the underlying background must be decided. In addition, the optimum location of the polar feature with respect to the disk center must be determined. Our two component model has a photometric centroid lying on the line joining the center of the planetary disk with the center of the polar feature.

Our initial step in the reconstruction of the Uranus image is to remove the slit function from the original scans of the planet. Simultaneous removal of both slit broadening and high frequency noise was achieved by an iterative Bayesian estimation technique developed by Lucy (1974). Numerical experiments with simulated slit scans of the planet showed that the original line projection could be recovered, with a peak signal-to-noise

ratio ~200:1 corresponding to a photometric accuracy ~0.5 percent. A maximum of three iterations was required. Figure 3 shows the orthogonal line projections of Uranus derived from the observational slit scan data.

On 1978 June 25, the Uranus geocentric distance was 17.972 A.U. If we assume Uranus to be spherical, the planetary radius (25,900 kms) determined by Danielson et al. (1972) gave an apparent angular diameter for the planet of 3".974 arc. Information provided by the American Ephemeris and Nautical Almanac shows that the visible pole of the planet was then located at a radial distance of 1".156 arc from the disk center in position angle 274°.51. More explicitly, the pole was located 1".152 arc west, and 0".091 arc north, of the disk center.

Detailed examination of the orthogonal line projections given in Figure 3 shows the S-N profile to be extraordinarily symmetric in contrast to the highly skewed E-W profile. To estimate the optimum position of the polar feature, we assumed that its center was located on the line joining the center of the disk with the projected geometrical pole. Using a relaxation technique, coupled with a least-squares' criterion for matching theory with observation, we determined the optimum properties of both components of the Uranus image. Energies contained in the background disk and in the polar feature were in the respective proportions 1:0.24. The optimum location of the polar component was determined to be at a radial distance of 0".092 arc from the center of the disk. Removal of the optimum polar feature from the orthogonal line projections of the planet permitted determination of the mean line projection of the background disk.

Theoretical reconstructions of the orthogonal line projections of the Uranus image are also shown in Figure 3. Detailed comparison of theory with observation shows that our simple two-component model is highly satisfactory. Scaled with respect to the centroid ordinate, the rms deviations for the S-N and E-W line projections are 0.55 and 0.73 percent respectively. But literal interpretation of the Uranus image model should be treated with caution. Our two-component model is strictly artificial. It exists only to provide a convenient mathematical description of the planetary image for use in the restoration method.

4. NUMERICAL RESTORATION

Our numerical restoration technique is based on a modification of the Fourier transform inversion method developed by Price and Franz (1979) specifically for the Uranus problem. Incoherent light is received from Uranus. Since formation of the image involves the superposition of two independent components, whose specific intensities are additive, it follows that each component may be separately restored. Superposition of the individual restorations will then complete restoration of the entire image.

Both components of the Uranus image are considered to be circularly symmetric although not concentric. Let us define the true intensity distribution over either image component, $g(r)$, the point spread function, $f(r)$, and the observed intensity distribution for the relevant component, $h(r)$. Making use of the Fourier transform convolution theorem, we can write

$$G(\rho) = H(\rho)/F(\rho) \tag{2}$$

where capitalization of the functions indicates their zeroth order Hankel transforms, and the variable ρ denotes spatial frequency. In principle, the original distribution, $g(r)$, can be recovered by taking the relevant inverse Hankel transform. Explicitly, we have

$$g(r) = 2\pi \int_0^\infty \rho \, \frac{H(\rho)}{F(\rho)} \, J_0 \, (2\pi r\rho) \, d\rho \tag{3}$$

where

$$H(\rho) = 2\pi \int_0^\infty r \, h(r) \, J_0 \, (2\pi r\rho) \, dr \tag{4}$$

and

$$F(\rho) = 2\pi \int_0^\infty r \, f(r) \, J_0 \, (2\pi r\rho) \, dr \tag{5}$$

where $J_0(2\pi r\rho)$ is the zeroth order Bessel function. But practical restoration contains two major potential pitfalls.

First, during restoration of the Uranus background disk, serious oscillations can be produced by the discontinuity at the edge of the planet unless the relevant true intensity, $g(r)$, is treated as a perturbation on a uniform disk. Both the Uranus background and the flat disk are assumed to be of equal angular extent, and to be smeared by identical point spread functions. Using the Fourier transform linearity theorem, together with an obvious subscript notation, we can rewrite equation (3) in the form

$$g_u(r) = g_F(r) + 2\pi \int_0^\infty \rho \frac{K(\rho)}{F(\rho)} J_0(2\pi r\rho)\, d\rho \tag{6}$$

where

$$K(\rho) = 2\pi \int_0^\infty r \left\{ h_u(r) - h_F(r) \right\} J_0(2\pi r\rho)\, dr \tag{7}$$

and

$$g_F(r) = \begin{cases} 1 & \text{for } r \leq R_u \\ 0 & \text{for } r > R_u \end{cases} \tag{8}$$

where R_u is the angular radius of Uranus at the time of observation. Both $h_u(r)$ and $h_F(r)$ must be normalized so that

$$2\pi \int_0^\infty r\, h_u(r)\, dr = 2\pi \int_0^\infty r\, h_F(r)\, dr = \pi R_u^2. \tag{9}$$

Smearing of the flat disk is conveniently described by the mathematical statement

$$h_F(r) = g_F(r) ** f(r) \tag{10}$$

where the double asterisk denotes two-dimensional convolution in signal space.

Second, filtering in the spatial frequency domain is required to control amplification of the residual photometric noise. Our filter must provide a weighting function which varies from unity at zero frequency to zero at a finite frequency. Suppose we denote the weighting function $S(\rho)$, and its Hankel transform $s(r)$. Since multiplication in frequency space is equivalent to convolution in signal space, the restored image will necessarily contain a residual smear viz, $s(r)$. Making use of the Fourier transform linearity theorem, we can rewrite equation (6) in the form

$$\bar{g}_u(r) = \bar{g}_F(r) + 2\pi \int_0^\infty \rho \, \frac{S(\rho)}{F(\rho)} \, K(\rho) \, J_0(2\pi r\rho) \, d\rho \tag{11}$$

where

$$\bar{g}_u(r) = g_u(r) ** s(r) \tag{12}$$

and

$$\bar{g}_F(r) = g_F(r) ** s(r) \tag{13}$$

so that

$$2\pi \int_0^\infty r \, \bar{g}_F(r) \, dr = \pi R_u^2 \tag{14}$$

by appropriate normalization of the weighting function $S(\rho)$. Equation (11) will serve as the basis of our numerical restoration of the Uranus background disk. By comparison, restoration of the polar feature is much more

straightforward. Its shape becomes simply that of the residual smear function alone.

Practical restoration of the Uranus background disk is concerned with the numerical evaluation of the ensemble of functions in equation (11). Making use of the Fourier transform convolution theorem, we can write

$$\bar{g}_F(r) = 2\pi \int_0^\infty \rho\ D(\rho)\ S(\rho)\ J_0\ (2\pi r\rho)\ d\rho \tag{15}$$

where $D(\rho)$, the Hankel transform of the uniform disk, is given by

$$D(\rho) = \frac{R_u}{\rho}\ J_1\ (2\pi\rho\ R_u) \tag{16}$$

where $J_1\ (2\pi\rho\ R_u)$ is the first order Bessel function. To evaluate the Hankel transform of the point spread function, we have the analytical form

$$F(\rho) = \frac{1}{\left\{A_p\sigma_{1p}{}^2 + B_p\sigma_{2p}{}^2\right\}} \cdot \left\{ A_p\sigma_{1p}{}^2 \cdot \exp\left[-\pi^2\sigma_{1p}{}^2\rho^2\right] \right.$$

$$\left. + B_p\sigma_{2p}{}^2 \cdot \exp\left[-\pi^2\sigma_{2p}{}^2\rho^2\right] \right\} . \tag{17}$$

Windowing in frequency space has been reviewed recently by Harris (1978). Restricting the bandwidth necessarily leads to "ripple" in signal space. To minimize the problem, we chose the well-know Hanning filter given by

$$S(\rho) = \begin{cases} \cos^2\ (\pi\rho/2\Omega) & \text{for } \rho \leq \Omega \\ 0 & \text{for } \rho > \Omega \end{cases} \tag{18}$$

where we have introduced the cut-off frequency Ω. Determining Ω requires the selection of a maximum enhancement factor, M, in the spatial frequency domain. Explicitly, we require

$$\underset{0 \leq \rho \leq \Omega}{\text{Max}} \left[S(\rho)/F(\rho)\right] = M \tag{19}$$

Equation (19) may be solved for Ω by a relaxation method. To evaluate $K(\rho)$, we rewrite equation (7) in the form

$$K(\rho) = H_u(\rho) - H_F(\rho) \tag{20}$$

where $H_u(\rho)$ and $H_F(\rho)$ are the respective Hankel transforms of the radial distributions of intensity for the Uranus background image and for the correspondingly smeared flat disk. Making use of the Fourier transform projection-slice theorem, in the manner discussed by Oppenheim, Frisk, and Martinez (1978), we may rewrite equation (20) in the form

$$K(\rho) = \int_{-\infty}^{+\infty} p_u(x) \cdot \exp\left[-2\pi j\rho x\right] dx - \int_{-\infty}^{+\infty} p_F(x) \cdot \exp\left[-2\pi j\rho x\right] dx \tag{21}$$

or

$$K(\rho) = \int_{-\infty}^{+\infty} \left\{ p_u(x) - p_F(x) \right\} \cdot \exp\left[-2\pi j\rho x\right] dx \tag{22}$$

where $p_u(x)$ and $p_F(x)$ are the respective one-dimensional projections, on an arbitrary x-axis, of the Uranus background image and of the corresponding smeared flat disk. The Uranus projection, $p_u(x)$, is the mean line projection of the background image derived in the reconstruction work. The flat disk projection, $p_F(x)$, may be calculated by the method given by Price and Franz (1978).

Written in the form of a discrete Fourier transform, equation (22) can be readily evaluated by the Cooley-Tukey (1965) algorithm. We chose a 512 point Fast Fourier Transform (FFT). Numerical evaluation of the integral in equation (11) requires information concerning the behavior of $K(\rho)$ between the FFT values computed for discrete spatial frequencies. On the assumption that the Uranus image is band-limited in signal space, interpolation may be carried out by means of the sampling theorem given by

$$K(\rho) = \frac{1}{2T} \sum_{n=-\infty}^{+\infty} K(n/2T) \; \frac{\sin\left[2\pi T\,(\rho - n/2T)\right]}{\pi\left[\rho - n/2T\right]} \qquad (23)$$

where T is the band-width taken equal to 256 times the sampling interval in signal space. Beyond a radial distance of 8".1, the Uranus image is assumed to have zero intensity. In equation (23), the summation was carried out over all discrete values of the FFT.

5. RESULTS

Maximum enhancement factors greater than 150-200 lead to unstable restorations through the unfortunate amplification of noise. Four restorations of the Uranus image are shown in Figure 4. Each panel corresponds to a distinct choice for the maximum enhancement factor in the range 25-100. Two radial profiles, chosen to emphasize the polar feature, were selected for each panel. A polar profile, passing through the center of both components of the Uranus image, is shown together with an orthogonal scan through the center of the planetary disk. For comparison purposes, the radial profile for a uniform disk, convolved with the appropriate residual smear function is also shown. Residual smear functions, corresponding to each restoration, are shown in Figure 5. A three-dimensional view of the restored Uranus image (M = 100) is shown in Figure 6. An isometric projection was used.

Spatial resolution within the restored profiles can be defined in a manner analogous to the Rayleigh limit in optical systems. Specifically, the resolution can be taken equal to the radius of the first zero of the residual smear function. If we adopt a maximum enhancement factor of 100, the corresponding spatial resolution is 0".9 arc.

Extraneous ripple in the restored profiles, beyond the edge of the planet, indicates the level of uncertainty remaining in the restorations. Significant polar and limb brightening are confirmed to be present on the Uranus disk in the 7300Å CH_4 band. If polar brightening were absent, the center-to-limb intensity ratio would be approximately 1:2, the optimum value derived by Price and Franz (1978). Peak polar, limb, and central intensities are, therefore, in the respective proportions 3:2:1. The theoretical interpretation reported by Price (1978) is placed on a much firmer foundation.

Detailed examination of Figure 4 shows that the restored polar feature is not located precisely on the projected pole. Its peak intensity occurs approximately mid-way between the disk center and the geometrical pole. Our two component model of the Uranus image indicated that the polar feature should lie much closer to the disk center. Outward displacement of the peak polar intensity in the restorations is caused by the steep gradient in the underlying limb brightened profile.

Physical location of the polar feature requires comment. Two explanations come to mind. If polar brightening is caused by an aerosol haze, the apparent displacement towards the disk center may be the result of interplay between the two major factors influencing atmospheric circulation: rotation and insolation. Price and Franz (1979) showed that such a polar haze would require an optical thickness $\sim$0.5 or greater. Or, partial visibility of the deep dense cloud layer near the disk center may be shifting the photometric centroid of the planet. Price and Franz (1979) then showed that the maximum permitted CH_4/H_2 mixing ratio in the visible atmosphere would correspond to $\sim$3 times the solar value. Further information concerning structure on the disk of the planet should be obtainable by direct two-dimensional imaging coupled with the application of an image restoration algorithm.

ACKNOWLEDGMENTS

This research was supported by the National Aeronautics and Space Administration under contract NASW-3134 and grant NGR-03-003-001. The equipment used to gather the photometric data was originally developed, assembled, and tested with the support of National Science Foundation grants GP-6983 and GP-20090.

REFERENCES

Avis, C.A., Smith, H.J., Bergstralh, J.T., and Sandmann, W.H. (1977), "Photometric Determination of the Rotation Period of Uranus," Paper presented at the Eighth Annual Meeting of the American Astronomical Society, Division for Planetary Sciences, Honolulu, Hawaii, 1977 January 19-22.

Cooley, J.W. and Tukey, J.W. (1965), "An Algorithm for the Machine Calculation of Complex Fourier Series," Math. of Computation 19, 297-301.

Danielson, R.E., Tomasko, M.G., and Savage, B.D. (1972), High resolution imagery of Uranus obtained by Stratoscope II. Astrophys. J. 178, 887-900.

Franz, O.G. and Price, M.J. (1977), "Uranus: Limb and Polar Brightening at λ7300Å," Astrophys. J. 214, L145-L146.

Harris, F.J. (1978), "On the Use of Windows for Harmonic Analysis with the Discrete Fourier Transform," Proc. IEEE 66, 51-83.

Lucy, L.B. (1974), "An Iterative Technique for the Rectification of Observed Distributions," Astron. J. 79, 745-754.

Mersereau, R.M. and Oppenheim, A.V. (1974), "Digital Reconstruction of Multidimensional Signals from their Projections," Proc. IEEE. 62, 1319-1338.

Oppenheim, A.V., Frisk, G.V., and Martinez, D.R.(1978), "An Algorithm for the Numerical Evaluation of the Hankel Transform," Proc. IEEE. 66, 264-265.

Price, M.J. (1978), "Limb-Brightening on Uranus: An Interpretation of the λ7300Å Methane Band," Icarus 35, 93-98.

Price, M.J. and Franz, O.G. (1976), "Limb-Brightening on Uranus: The Visible Spectrum," Icarus 29, 125-136.

Price, M.J. and Franz, O.G. (1978), "Limb-Brightening on Uranus: The Visible Spectrum, II," Icarus 34, 355-373.

Price, M.J. and Franz, O.G. (1979), "Uranus: Narrow-Waveband Disk Profiles in the Spectral Region 6000-8500 Angstroms," Icarus (in press).

Sinton, W.M. (1972), "Limb and Polar Brightening of Uranus at 8870Å," Astrophys. J. 176, L131-L133.

Smith, B.A. (1977), "Uranus Photography in the 890-nm Absorption Band of Methane," Paper presented at the Eighth Annual Meeting of the American Astronomical Society, Division for Planetary Sciences, Honolulu, Hawaii, 1977 January 19-22.

Westphal, J.A. (1972), Comment at the Third Annual Meeting of the American Astronomical Society, Division for Planetary Sciences, Kona, Hawaii, 1972 March 21-24.

FIGURE CAPTIONS

Fig. 1. Stellar Slit Scans: Comparison of Theory with Observation. Composite observational data are shown by the solid curve; the best-fitting theoretical curve (described in the text) is shown by the broken curve. The slit width was 0.645 sec. arc; the sample interval was 0.032 sec. arc.

Fig. 2. Orthogonal Composite Uranus Slit Scans. Observational data for both south-north (SN) and east-west (EW) directions are shown. The zero point on the abscissa scale is taken as the photometric centroid of the scan. The slit width was 0.645 sec. arc; the sample interval was 0.032 sec. arc. Both scans are normalized to the same integrated energy.

Fig. 3. Orthogonal Line Projections of the Uranus Image. Both south-north (SN) and east-west (EW) projections are shown. Theoretical reconstructions (broken curves) are compared with the smoothed and rectified observational data (solid curves). The zero point on the abscissa scale is taken to be the centroid of the photometric projection. Both projections are normalized to the same integrated energy.

Fig. 4. Uranus: Selected Restorations. Results for four choices of the maximum enhancement factor (M) are shown. But only one pair of radial profiles (solid curves) is shown for each choice. The polar profile (P.A. 274.51 degrees) is given together with the symmetrical orthogonal profile (P.A. 184.51 degrees). In each panel, a uniform planetary disk subjected to the corresponding residual smear function is shown by the broken curve. Within each panel, all profiles are normalized to the same total energy, obtained by integrating over the disk of the planet. The zero point of the abscissa scale corresponds to the center of the Uranus disk. For comparison, the unsmeared Uranus angular radius was 1.987 sec. arc., while the geometrical pole was located 1.156 sec. arc. from the disk center (P.A. 274.51 degrees).

Fig. 5. Residual Smear Functions corresponding to the maximum enhancement factors (M) selected in Fig. 4.

Fig. 6. Isometric diagram giving a three-dimensional rendition of the optimum Uranus restoration (M = 100). Each axis in the plane of the sky has a length of 10 sec. arc. In order to simplify the plot, all intensities at radial distances greater than 5 sec. arc. from the center of the disk have been set equal to zero.

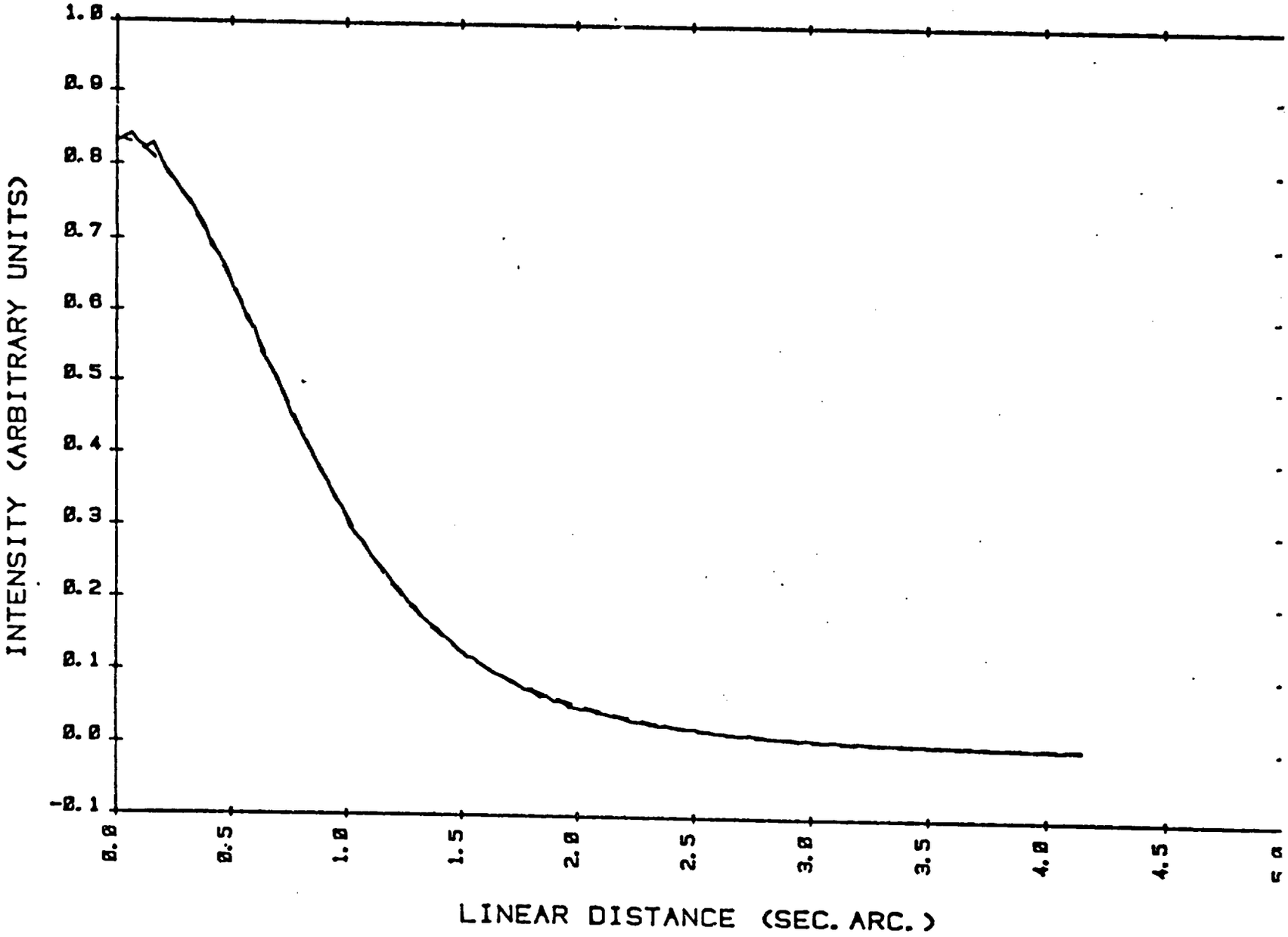
INTENSITY (ARBITRARY UNITS)
1.0
0.9
0.8
0.7
0.6
0.5
0.4
0.3
0.2
0.1
0.0
-0.1
0.0
0.5
1.0
1.5
2.0
2.5
3.0
3.5
4.0
4.5
LINEAR DISTANCE (SEC. ARC.)

Fig. 1

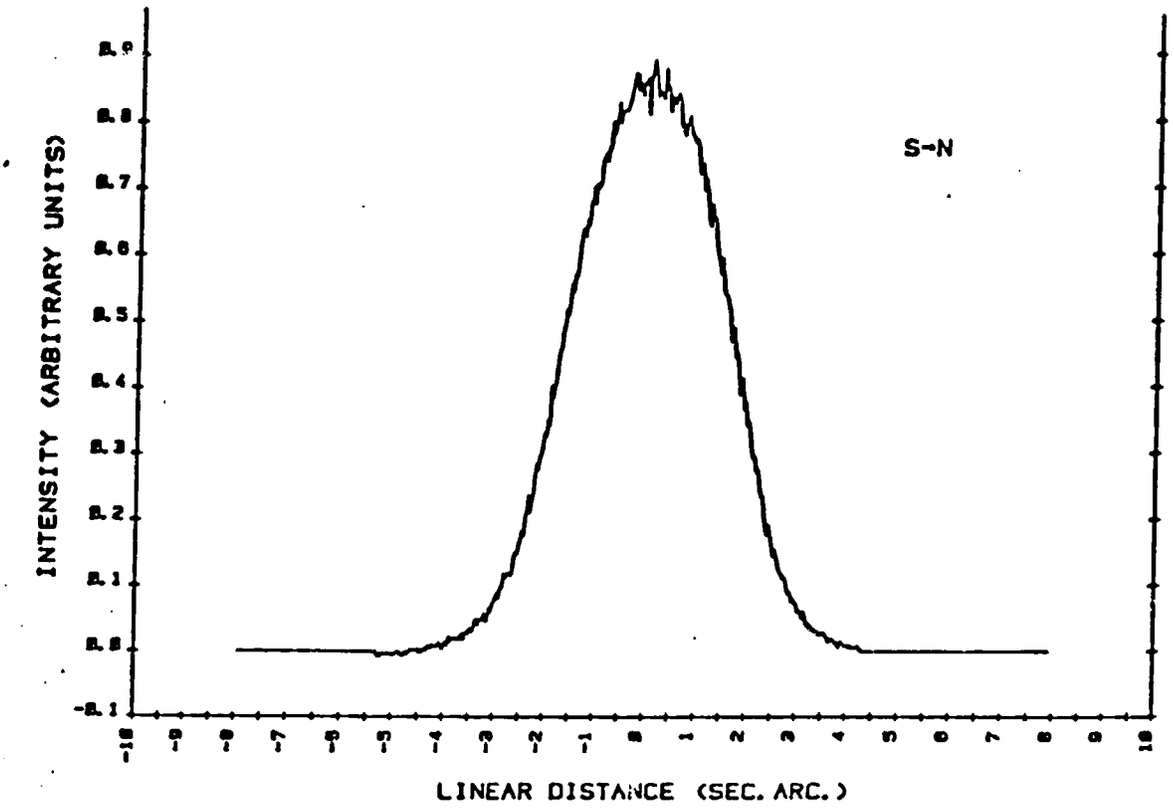
S-N
INTENSITY (ARBITRARY UNITS)
LINEAR DISTANCE (SEC. ARC.)

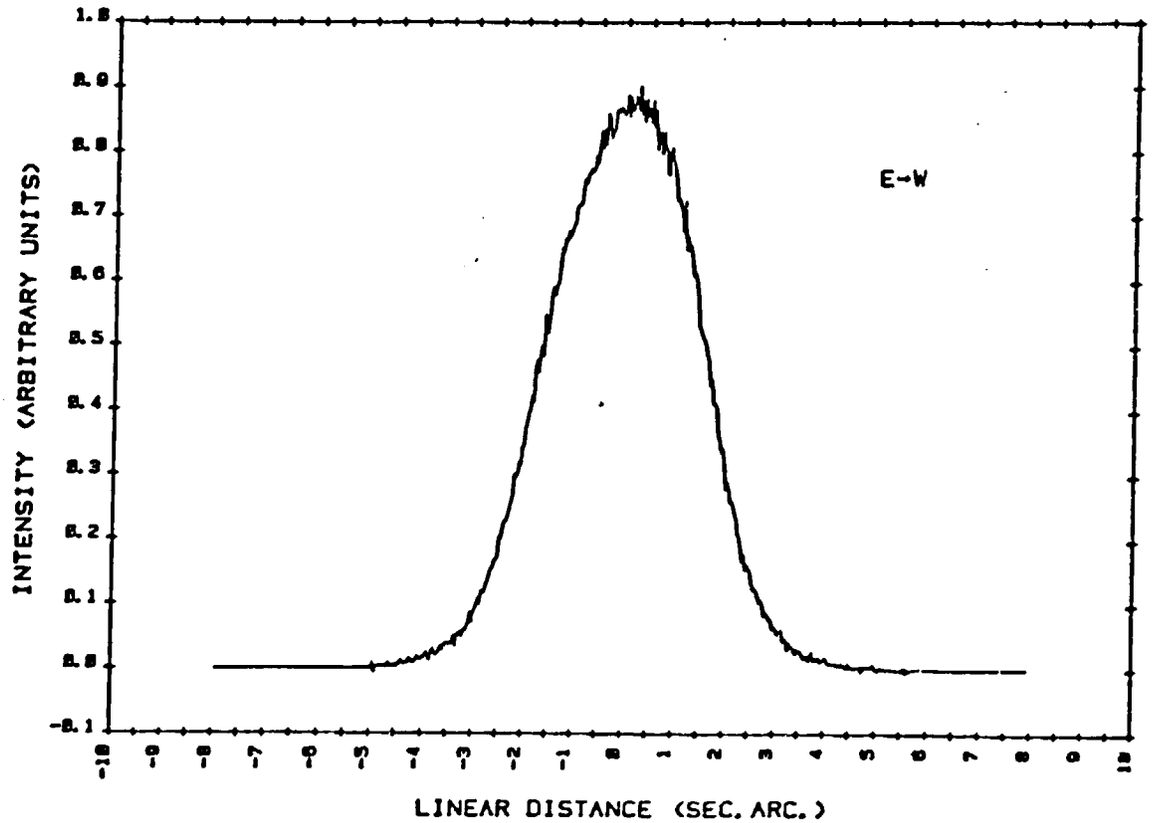
E-W
INTENSITY (ARBITRARY UNITS)
LINEAR DISTANCE (SEC. ARC.)

Fig. 2

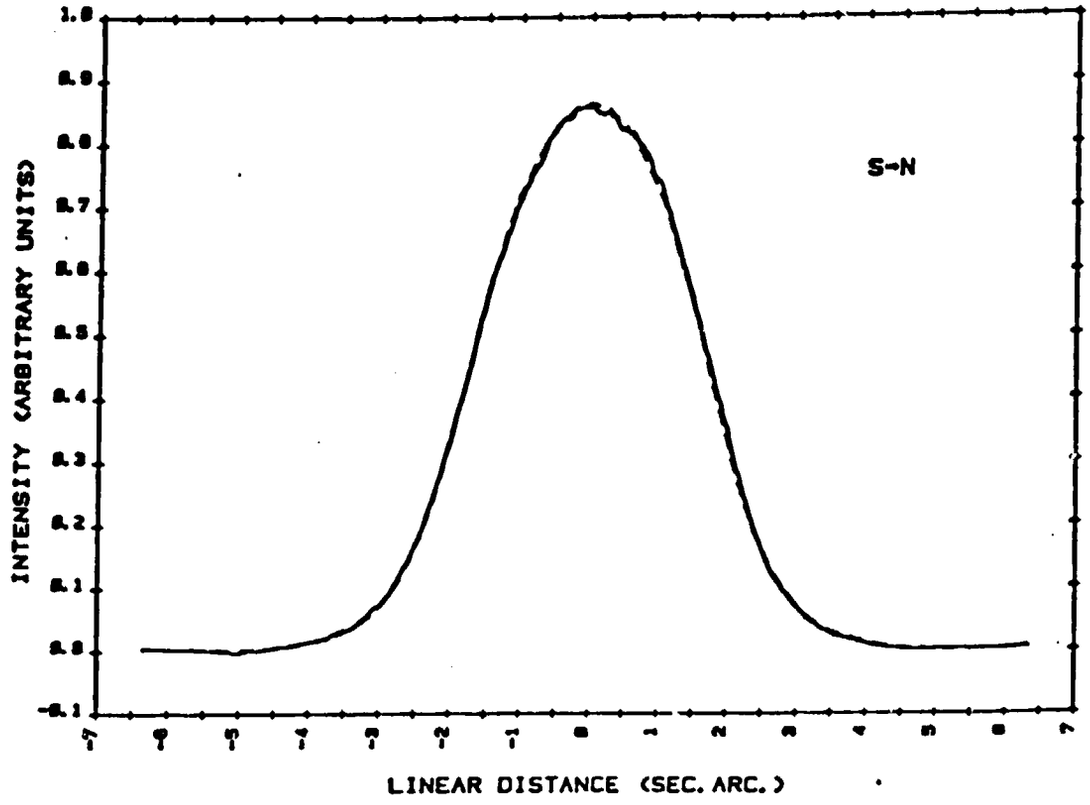
S-N
INTENSITY (ARBITRARY UNITS)
LINEAR DISTANCE (SEC. ARC.)

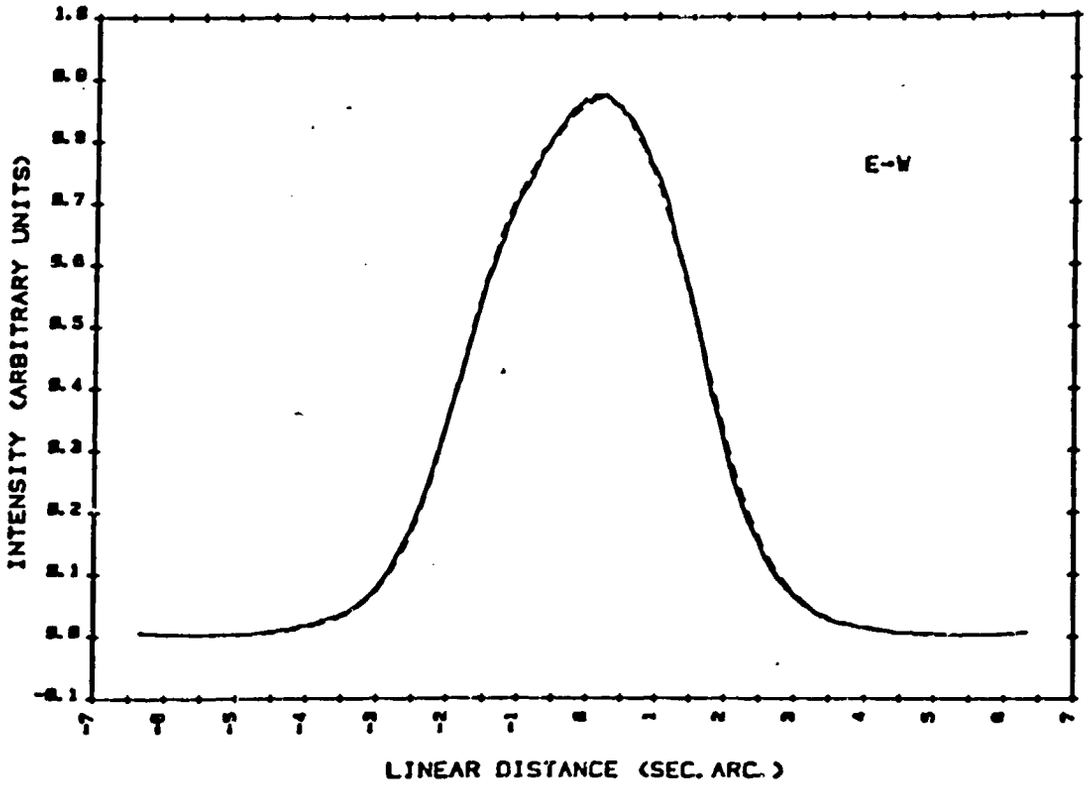
E-W
INTENSITY (ARBITRARY UNITS)
LINEAR DISTANCE (SEC. ARC.)

Fig. 3

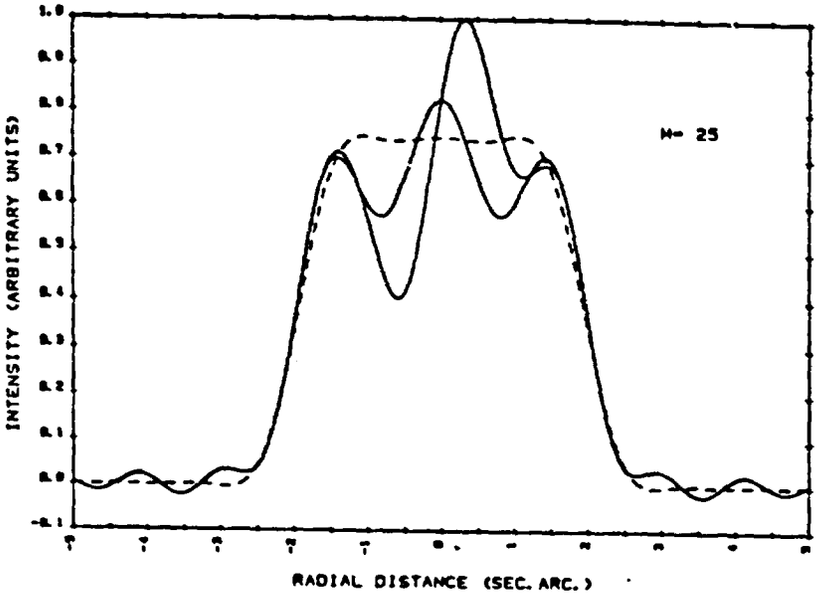
M= 25
INTENSITY (ARBITRARY UNITS)
RADIAL DISTANCE (SEC. ARC.)

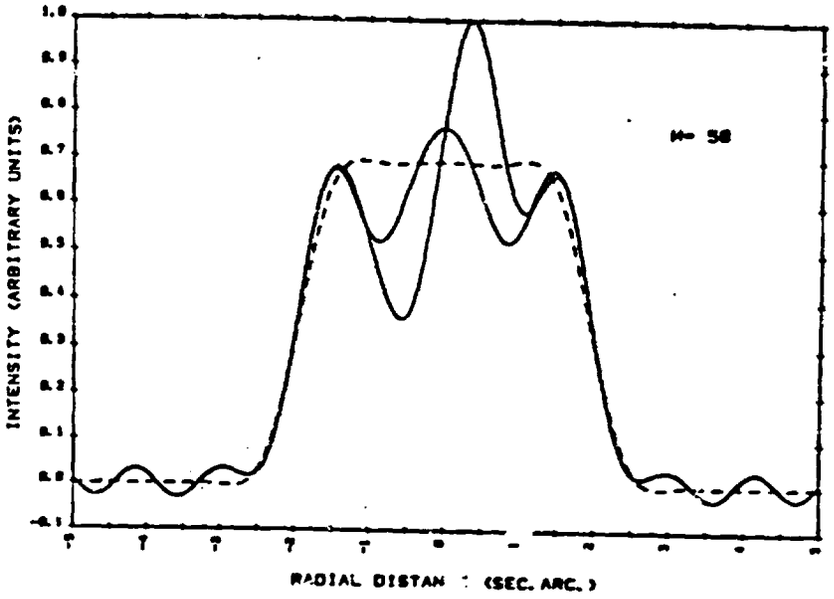
M= 50
INTENSITY (ARBITRARY UNITS)
RADIAL DISTANCE (SEC. ARC.)

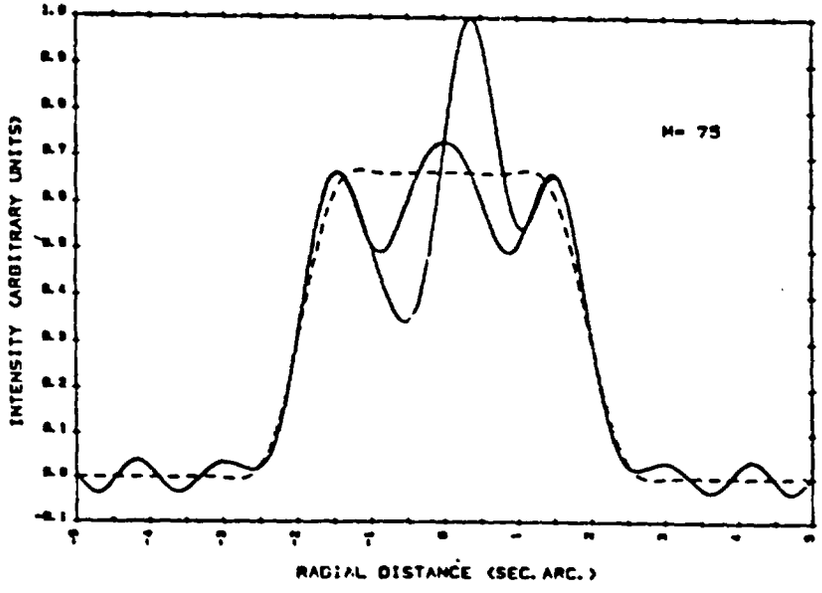
M= 75
INTENSITY (ARBITRARY UNITS)
RADIAL DISTANCE (SEC. ARC.)

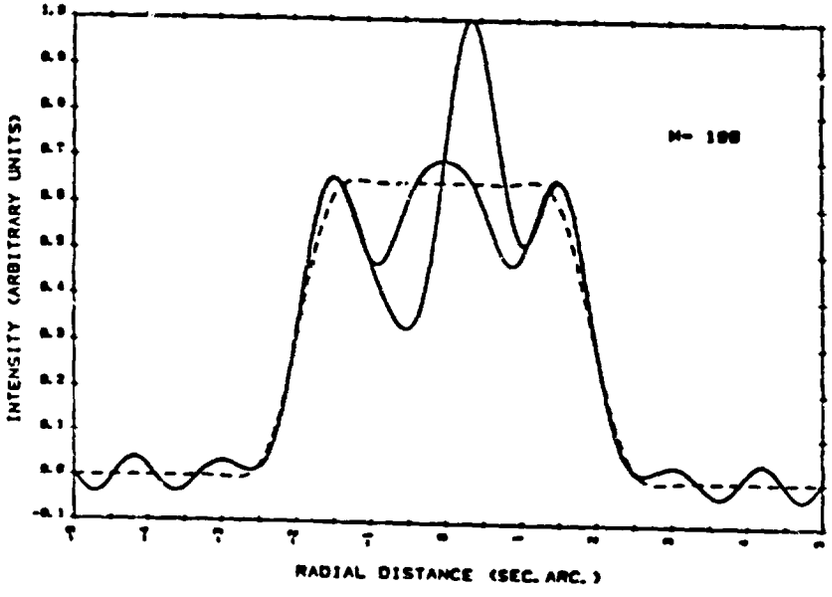
M= 100
INTENSITY (ARBITRARY UNITS)
RADIAL DISTANCE (SEC. ARC.)

Fig. 4

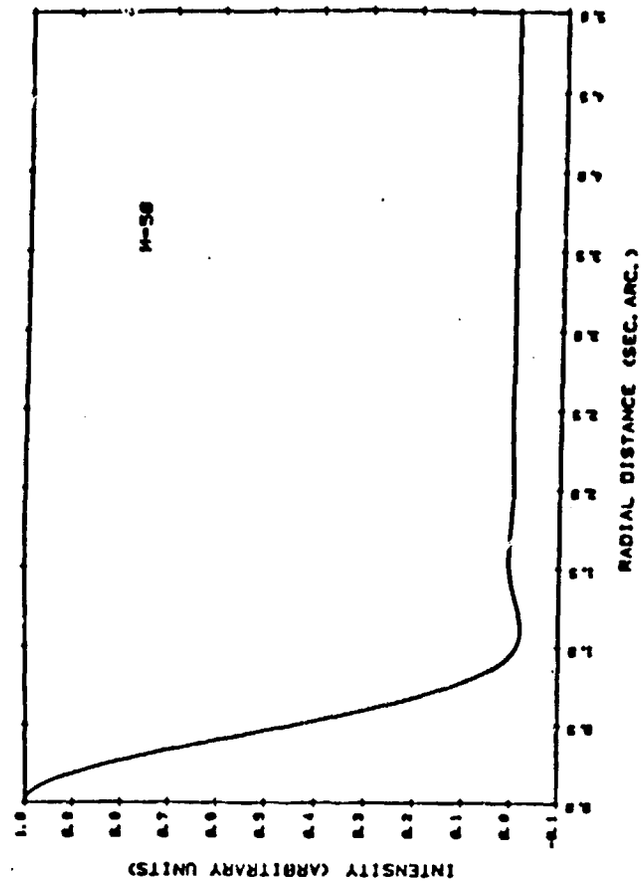
M=50
INTENSITY (ARBITRARY UNITS)
RADIAL DISTANCE (SEC. ARC.)

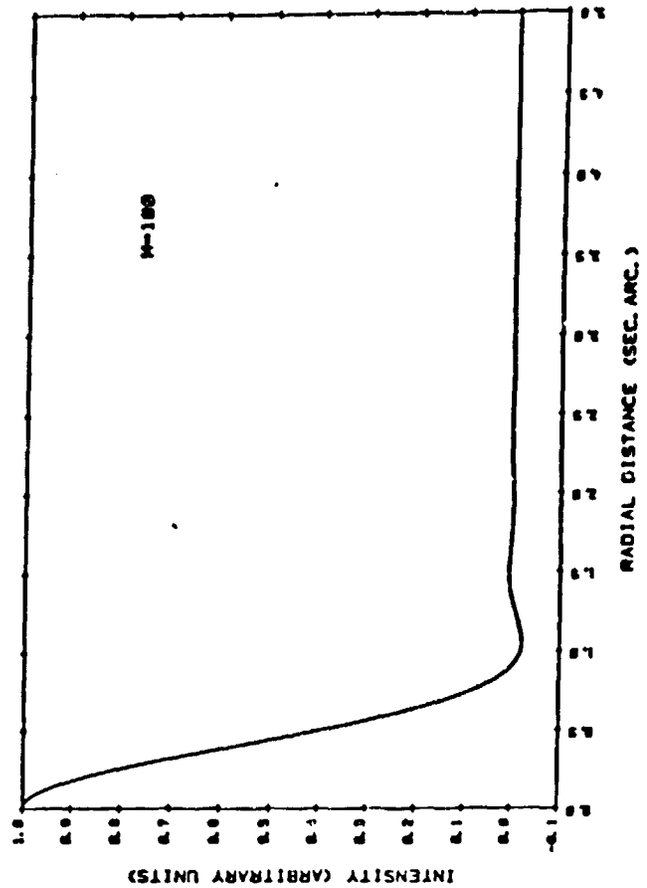
M=100
INTENSITY (ARBITRARY UNITS)
RADIAL DISTANCE (SEC. ARC.)

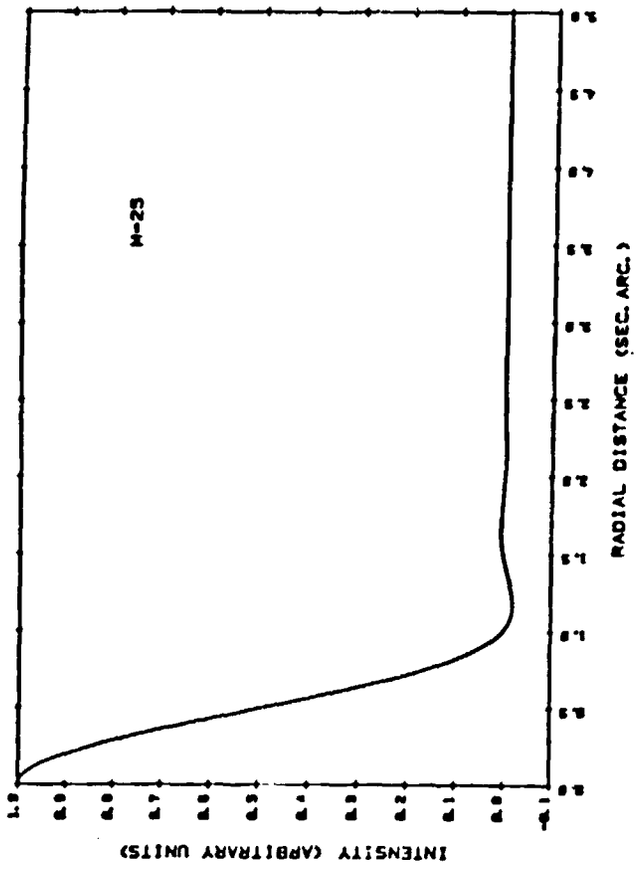
M=25
INTENSITY (ARBITRARY UNITS)
RADIAL DISTANCE (SEC. ARC.)

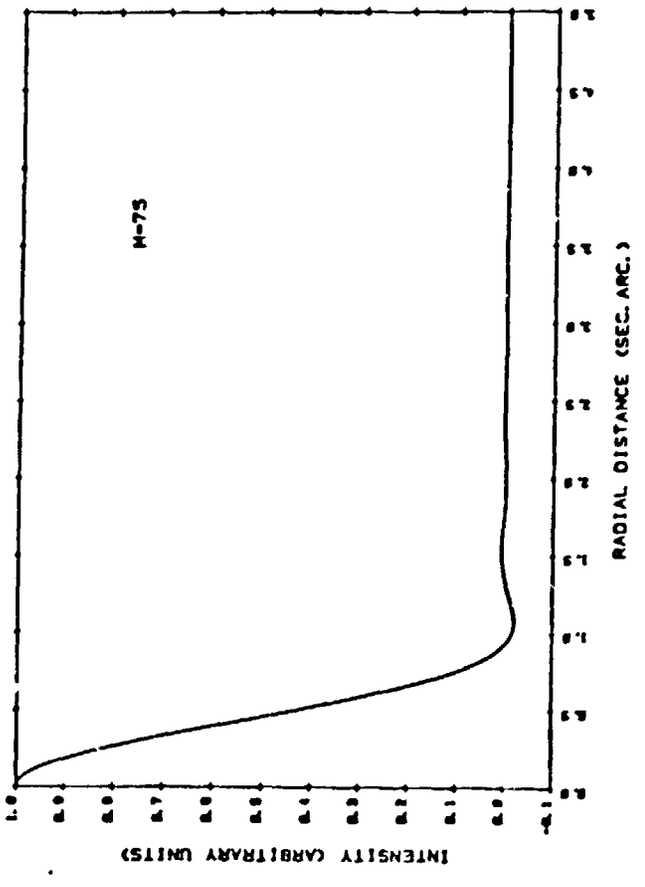
M=75
INTENSITY (ARBITRARY UNITS)
RADIAL DISTANCE (SEC. ARC.)

Fig. 5

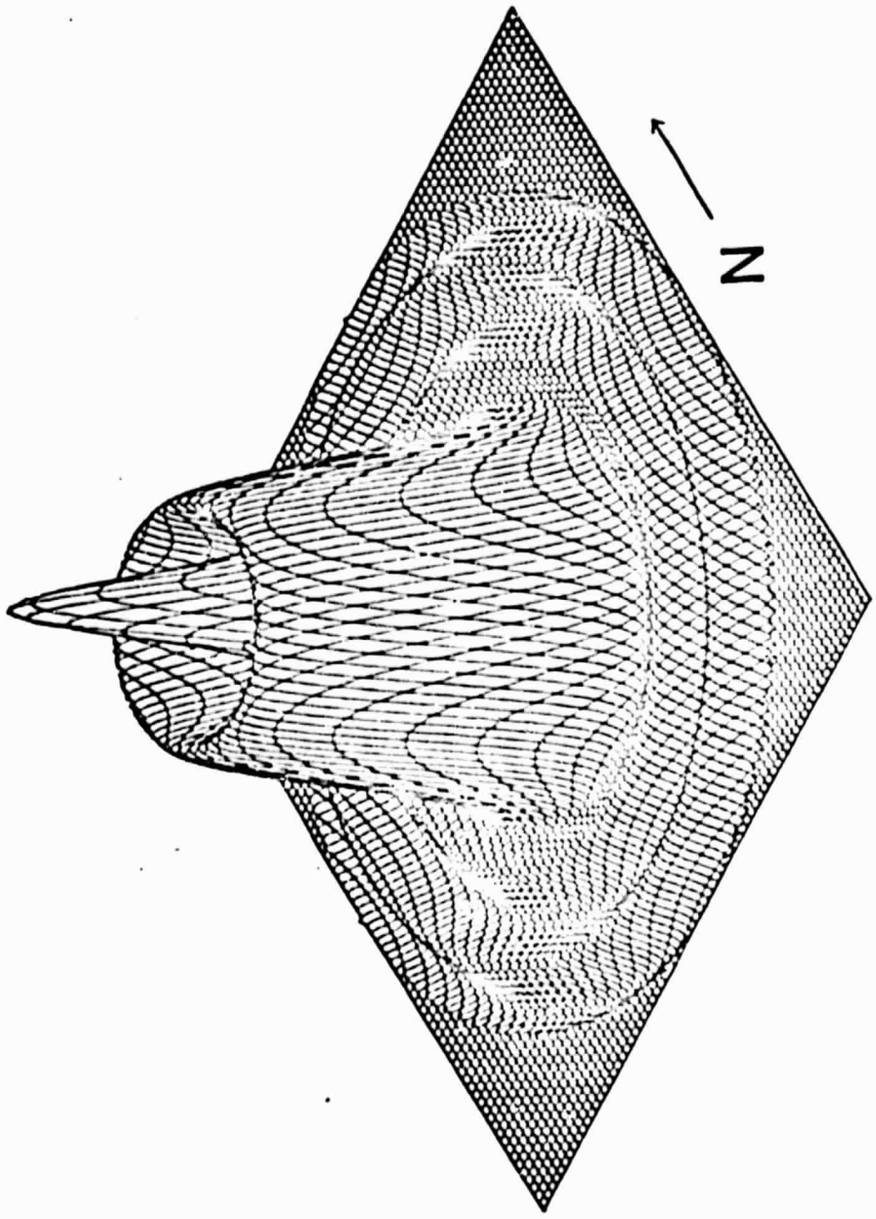

Fig. 6

APPENDIX C

NEPTUNE: LIMB BRIGHTENING WITHIN THE 7300 ANGSTROM METHANE BAND

Michael J. Price
Science Applications, Inc.
5055 E. Broadway, Suite A-214
Tucson, Arizona 85711

and

Otto G. Franz
Lowell Observatory
P.O. Box 1269
Flagstaff, Arizona 86002

No. of Copies: 4

No. of MS Pages: 20

No. of Figures: 5

No. of Tables: 2

ABSTRACT

Narrow-waveband (100Å) photoelectric slit scan photometry of the Neptune disk is reported. Observations were concentrated within the strong CH_4 band at λ7300Å. For comparison, measurements were also made within a continuum waveband at λ6800Å. Point spread function data were obtained in both colors. Qualitative estimates of the true intensity distribution over the Neptune disk were made. Within the λ6800Å continuum band, Neptune appears as an essentially uniform disk. Within the λ7300Å CH_4 band, the planet exhibits strong limb-brightening. Our results appear to require the presence of an optically thin layer of brightly scattering aerosol particles high in the Neptune atmosphere.

1. INTRODUCTION

Trafton (1974) reported the first measurements of the H_2 quadrupole lines in the spectrum of Neptume. Strengths of the S(0) and S(1) lines of the (4-0) band were interpreted in terms of both an inhomogeneous atmosphere overlying a reflecting layer, and a homogeneous, semi-infinite scattering atmosphere. Only the scattering model proved to be consistent with Neptune's spectrum in this wavelength region. The H_2 abundance along a scattering mean free path was found to be $\sim$ 320 km. amagat; the maximum permitted abundance was 450 km. amagat. By comparison, the scattering mean free path for Rayleigh scattering in a pure H_2 atmosphere is equivalent to 715 km. amagat. Although aerosol particle scattering may be responsible for the observed reduction in the mean free path, Trafton noted that an alternative explanation might be molecular scattering from gases additional to hydrogen. From an analysis of photoelectric photometry of Neptune, Lockwood (1978) concluded that the scattering properties of the atmosphere are variable, and that aerosol particles are present.

Infrared (1-4 μm) observations of Neptune have been interpreted by Joyce et al. (1977) and by Pilcher (1977) to suggest that, over a one year period, an extensive high altitude cloud formed on the planet and then partially dissipated. About 10-months after its initial appearance, the optical thickness of the cloud averaged over the planet was on the order of unity. An H_2 column-abundance of 5 ± 2 km. amagat was derived; it appeared to refer to an effective reflecting layer high in the atmosphere of Neptune.

Recent infrared (0.8 - 2.5 μm) studies of Neptune by Fink and Larson (1979) have indicated that its atmosphere has a variable height cloud layer overlain by $\sim$ 50 km. amagat of H_2. Fink and Larson point out that the high cloud layer cannot have a large optical thickness since both the H_2 quadrupole lines and the visible CH_4 bands give quite large abundances. Specifically, the CH_4 column abundance was found to be $\sim$ 0.7 km. amagat. For Uranus, the corresponding value was 1.6 km. amagat. Fink and Larson also found the Uranus atmosphere to be clear to great depths with its upper

regions depleted in CH_4. It appears likely that visible radiation can probe to great depths in the Neptune atmosphere.

Useful information concerning the opacity of the Neptune atmosphere, in particular the presence of an optically thin upper cloud layer, can be derived from measurements of the distribution of intensity over the disk of the planet both within and between the strong CH_4 bands. In this paper, we report the first attempt to infer the wavelength-dependent optical appearance of the Neptune disk.

2. OBSERVATIONS

During the 1979 Neptune apparition, narrow-band (100Å) slit scan photometry of the planet was carried out within two regions of the spectrum by the technique described by Price and Franz (1979). Scans were obtained primarily within the 7300Å CH_4 band. But, for comparison, scans were also made within the continuum region at 6800Å. Waveband selection was achieved by means of two filters used in our early investigation of Uranus (Price and Franz: 1976). On 1979 July 23, reliable observational data were obtained with the area-scanner mounted on the 1.8 meter Perkins reflector at Lowell Observatory.

Neptune was difficult to observe because of its extreme southerly declination (-21 degrees). Even at meridian transit, the planet never reached an elevation angle greater than $\sim$ 33 degrees. In order to minimize the path length through the atmosphere, observations were restricted to within $\pm$ 2 hours of transit. Effects of differential refraction, both within and between each waveband, were avoided by orienting the slit length in a north-south direction. Both the stellar and Neptune images would then suffer dispersion along the slit when observations were made near the meridian. Special care was taken in the determination of the point spread function. A star, of apparent visual magnitude $\sim$ 7.0, located within 45 arc. min. of Neptune, at an elevation angle essentially identical with that of the planet, was selected to provide PSF information. Both Neptune and the star were scanned in an east-west direction only. Both forward and reverse scans were used. Samples were taken at spatial intervals of 0.032 arc. sec with a slit of 100 μm (0.645 arc. sec) width. Both slit and scan length were 2mm (12.9 arc. sec).

Each recorded scan of Neptune and of the star was obtained by integrating 100 one-second scans. Shortening the integration time, although desirable to minimize image wander produced by telescope tracking errors and by variations in atmospheric refraction, would have adversely affected the signal-to-noise ratio. If image wander did occur, we hoped to match

its effects for both Neptune and the star by equalizing their integration times. To increase the effective signal-to-noise ratio, composites of the integrated scans were subsequently computed by the method described by Price and Franz (1979). Scans made in opposite directions were mirrored on their centroids prior to computer summation. Both the Neptune and stellar composite scans were symmetrical within the level set by the residual photometric noise. Total scan numbers for both the Neptune and stellar composites are shown in Table I. Final Neptune and stellar slit scans were formed by averaging the respective composites about their centroids.

Atmospheric turbulence, together with diffuse instrumental scattering, is responsible for the observed point spread function. Our earlier investigations of Uranus (Price and Franz: 1978, 1979) showed that the point spread function is well represented by the summation of two colocated but distinct Gaussian curves. Normalizing the point spread function, f(r), to unit total energy, we can write its radial distribution in the form

$$f(r) = \frac{1}{\pi \left[A\sigma_1^2 + B\sigma_2^2\right]} \left\{A \exp\left[-r^2/\sigma_1^2\right] + B \exp\left[-r^2/\sigma_2^2\right]\right\} \qquad (1)$$

where A, B, σ_1 and σ_2 are constants. Optimum sets of PSF parameters for both wavebands were obtained from the composite stellar slit scans by the method described by Price and Franz (1979). Within the 6800Å waveband, we found A = 1, B = 0.1336, σ_1 = 0.9829 arc. sec, and σ_2 = 2.0730 arc. sec. Within the 7300Å waveband, we found A = 1, B = 0.1378, σ_1 = 0.9829 arc. sec, and σ_2 = 2.0413 arc. sec. As one would expect, the point spread function became narrower with increasing wavelength. Our best-fitting analytical scans are compared with the observational data in Figures 1 and 2 for the 6800Å and 7300Å wavebands, respectively. Scaled with respect to each central intensity, the respective root mean square deviations between calculation and observation are 0.62 percent and 0.68 percent. Evidently, the goodness-of-fit in each case is limited by the residual noise in the photometric data. Stability of the point spread function during the course of the observations was high. Consider both sets of PSF data

Table I

FORMATION OF COMPOSITE STELLAR AND NEPTUNE SLIT SCANS

Waveband (Angstroms)	Scan Object	Integrated Scans	One-Second Sweeps
6800	Star	2	200
	Neptune	4	400
7300	Star	2	200
	Neptune	8	800

together. The Gaussian 1/e-widths of the individual integrated stellar slit scans exhibited an rms deviation equivalent to 2.0 percent of the mean. Residual uncertainty in the mean point spread function for each waveband will have a negligible effect on the interpretation of the planetary data.

3. ANALYSIS

Careful examination of the Neptune slit scan data showed the level of the residual photometric noise to be too high to permit reliable restoration of the actual radial intensity distribution over the disk. Instead, we chose to qualitatively investigate the appearance of the planet by comparing the observed slit scans directly with predictions made for a variety of model intensity distributions. Our approach was first to model both the size and shape of the planet and to adopt a candidate radial distribution of intensity over the disk, next to employ the known point spread function in a two-dimensional convolution to derive the planetary image smeared by atmospheric seeing, then to compute the profile which would result from slit scanning the image in one-dimension (E-W), and finally to normalize the slit scan prediction to permit comparison with the observational data. Mathematical procedures developed by Price and Franz (1978) were used.

From stellar occultation data, Freeman and Lyngå (1970) found Neptune to be oblate, with an equatorial radius of 25265 $\pm$ 36 kms and an ellipticity of 0.026 $\pm$ 0.005. Their data refer to a level in the atmosphere corresponding to a molecular number density in the range 10^{12} to 10^{13} cm^{-3}. Assuming the Neptune atmosphere to be isothermal, Freeman and Lyngå derived an equatorial radius of 24753 $\pm$ 59 kms at a molecular number density of 10^{20} cm^{-3} where they expected a dense cloud layer to form. But, whether or not the Neptune atmosphere is indeed clear to such a depth is uncertain. For our present analysis, we adopted an equatorial radius of 25,000 kms. Effects of oblateness remain to be evaluated. Detailed consideration of both the observational geometry and technique showed that accurate theoretical slit scans of Neptune could be derived if the planetary disk were assumed to be perfectly circular with a radius equivalent to 0.994 times the equatorial value. Since the Neptune radius, relevant to our analysis, is not known within an accuracy of 0.5 percent, we chose to ignore the correction for oblateness. Neptune was taken to

be perfectly spherical with a radius of 25,000 kms. The American Ephemeris and Nautical Almanac gives the geocentric distance of Neptune on 1979 July 23 as 29.515 AU. The corresponding angular radius of the planet was 1.168 arc. sec.

Six simple models were adopted for the actual distribution of intensity over the Neptune disk. Circular symmetry was adopted throughout. In five models, the intensity was assumed to be a linear function of radial distance from the center of the disk. Each model was defined by the ratio of the intensities at the center and limb of the planet (CTL). A complete range of intensity distributions, from strong limb darkening through a flat disk to strong limb brightening, was considered. A sixth model represented the most extreme situation of limb brightening with the intensity assumed to be zero except within a ring of infinitesimal width located at the limb. Characteristics of the six models are summarized in Table II.

Theoretical Neptune slit scans are compared in Figure 3. All six models have been normalized to the same integrated energy. In general, the computations were based on mathematical procedures developed by Price and Franz (1978). But, for the ring of infinitesimal width, the radial intensity distribution of the smeared image was calculated by the method described in an Appendix. For both wavebands observed, the point spread functions are very similar. We therefore adopted a mean PSF for the comparison of the individual models. Specifically, its parameters were A = 1, B = 0.1357, σ_1 = 0.9829 arc. sec and σ_2 = 2.0572 arc. sec. In spite of the small angular diameter of the Neptune disk, strong limb-darkening or limb-brightening would be detectable if present. Note that the predicted scan intensity is essentially independent of the disk model at ~0.8 arc. sec from the profile center.

In Figures 4 and 5, observed Neptune slit scan data are compared with theoretical predictions for the 6800Å and 7300Å wavebands respectively. To avoid cluttering the diagrams, theoretical predictions are plotted only for the flat disk and for the ring of infinitesimal width. Predictions were based on the individual point spread functions relevant to each waveband. Both the observational data and theoretical predictions have

Table II

MODEL INTENSITY DISTRIBUTIONS FOR THE NEPTUNE DISK

Model	CTL
1	1:0
2	1:0.5
3	1:1
4	0.5:1
5	0:1
6	Ring

been normalized to the same integrated energy. By inspection, we conclude that Neptune is well represented by a flat disk at 6800Å, while strong limb-brightening is clearly present within the 7300Å CH_4 band. The degree of limb-brightening, however, cannot be determined accurately because of residual photometric noise.

Where the profiles are insensitive to the disk model, the observed and theoretical scans are very well matched. This consistency is most significant. It implies that tracking errors were negligible during acquisition of the Neptune data, that the radius of the planet was properly chosen, and that the observed point spread function provided an accurate description of atmospheric smearing of the disk.

4. DISCUSSION

Limb-brightening on Neptune must be the result of a vertical inhomogeneity in its atmosphere. More specifically, the single scattering albedo must decrease inversely with optical depth. Within the 7300Å CH_4 band, two explanations of the limb-brightening phenomenon are feasible. In the absence of aerosol particles, limb-brightening may be the result of methane depletion in the upper regions of the atmosphere. But, if the CH_4/H_2 mixing ratio is constant with optical depth, limb-brightening may be caused by an optically thin layer of aerosol particles high in the Neptune atmosphere. Hybrid explanations are also possible.

Within the 6800Å continuum waveband, limb-darkening would be expected to occur if the atmosphere were homogeneous. In a clear H_2 - CH_4 atmosphere, vibrational Raman scattering from molecular hydrogen would reduce the monochromatic single scattering albedo significantly below unity. Absorption from a weak CH_4 band at 6825Å would also contribute to a reduction in the single scattering albedo. Within this methane band, Giver (1978) found pressure effects to be insignificant. So no vertical inhomogeneity would result. For Neptune to appear as an essentially uniform disk, a limb-brightening mechanism must be acting to counter the natural tendency to limb-darkening. Such a mechanism could well be the presence of an optically thin layer of brightly scattering aerosol particles at high altitude. In fact, to reconcile our observational results with those obtained by other techniques, such a scattering layer appears to be essential. But whether or not the aerosol haze is laterally homogeneous cannot yet be determined.

APPENDIX

ATMOSPHERIC SMEARING OF A RING OF INFINITESIMAL WIDTH

Consider the situation of extreme limb brightening on a perfectly circular planetary disk. Suppose that all the radiation reflected by the planet is concentrated within a ring of infinitesimal width and with a radius equal to that of the disk itself. Normalizing the total radiant energy to unity, we can define the radial intensity distribution, g(r), in terms of the delta function. Specifically, we can write

$$g(r) = \frac{1}{2\pi a}\ \delta(r - a) \tag{A-1}$$

where a is the radius of the planetary disk. Suppose further, that atmospheric turbulence produces a smear described by a circularly symmetric point spread function, f(r), of the form

$$f(r)\ \frac{1}{\pi\left[A\sigma_1^{\,2} + B\sigma_2^{\,2}\right]} \cdot \left\{A \exp\left[-r^2/\sigma_1^{\,2}\right] + B \exp\left[-r^2/\sigma_2^{\,2}\right]\right\} \tag{A-2}$$

where A, B, σ_1 and σ_2 are constants which may be determined from observational data. Convolution of the point spread function, f(r), with the degenerate annulus, g(r), will produce a circularly symmetric image whose radial intensity distribution, h(r), may be readily computed.

Making use of the Fourier transform convolution theorem, we can write

$$H(\rho) = G(\rho) \cdot F(\rho) \tag{A-3}$$

where capitalization of the functions indicates their zeroth order Hankel transforms, and the variable ρ denotes spatial frequency. Explicitly, we have

$$F(\rho) = \frac{1}{[A\sigma_1^2 + B\sigma_2^2]} \cdot \left\{ A\sigma_1^2 \cdot \exp[-\pi^2\sigma_1^2\rho^2] + B\sigma_2^2 \cdot \exp[-\pi^2\sigma_2^2\rho^2] \right\} , \quad \text{(A-4)}$$

and

$$G(\rho) = J_0(2\pi a\rho) \quad \text{(A-5)}$$

where the symbol J_0 denotes the zeroth order Bessel function.

But, the radial intensity distribution of the image can be written

$$h(r) = 2\pi \int_0^\infty \rho\, H(\rho)\, J_0(2\pi r\rho)\, d\rho \quad . \quad \text{(A-6)}$$

Substituting equations (A-3), (A-4) and (A-5) into equation (A-6), we obtain

$$h(r) = \frac{2\pi}{[A\sigma_1^2 + B\sigma_2^2]} \left\{ A\sigma_1^2 \cdot T_1 + B\sigma_2^2 \cdot T_2 \right\} , \quad \text{(A-7)}$$

where

$$T_k = \int_0^\infty \rho\, J_0(\alpha\rho)\, J_0(\beta\rho) \cdot \exp[-\theta_k^2\rho^2]\, d\rho , \quad \text{(A-8)}$$

where

$$\left.\begin{aligned} \alpha &= 2\pi a \\ \beta &= 2\pi r \\ \theta_k &= \pi\sigma_k \end{aligned}\right\} . \quad \text{(A-9)}$$

Equation (A-8) is of a standard form tabulated by Gradshteyn and Ryzhik (1965). Explicitly, we have

$$T_k = \frac{1}{2\pi^2\sigma_k^2} \cdot \exp\left[-a^2/\sigma_k^2\right] \cdot \exp\left[-r^2/\sigma_k^2\right] \cdot I_0\left(2ar/\sigma_k^2\right) \qquad \text{(A-10)}$$

where the symbol I_0 denotes the modified Bessel function of the first kind of zeroth order. Formulae for the computation of I_0 are given by Abramowitz and Stegun (1972).

ACKNOWLEDGMENTS

This research was supported by the National Aeronautics and Space Administration under contract NASW-3134 and grant NGR-03-003-001. The equipment used to gather the photometric data was developed, assembled, and tested with the support of National Science Foundation grants GP-6983 and GP-20090.

REFERENCES

Abramowitz, M. and Stegun, I.A. (1972), "Handbook of Mathematical Functions," Dover: New York.

Fink, U. and Larson, H.P. (1979), "The Infrared Spectra of Uranus, Neptune, and Titan From 0.8 to 2.5 Microns," Astrophys. J. 233 (In press).

Freeman, K.C. and Lyngå, G. (1970), "Data for Neptune From Occultation Observations," Astrophys. J. 160, pp. 767-780.

Giver, L.P. (1978), "Intensity Measurements of the CH_4 bands in the Region 4350Å to 10,600Å," J. Quant. Spectrosc. Radiat. Transfer, 19, pp. 311-322.

Gradshteyn, I.S. and Ryzhik, I.M. (1965), "Tables of Integrals, Series, and Products," Fourth Edition, Prepared by Yu. V. Geronimus and M. Yu. Tseytlin, Translation Ed. A. Jeffrey, Academic Press, New York.

Joyce, R.R., Pilcher, C.B., Cruikshank, D.P., and Morrison, D. (1977), "Evidence for Weather on Neptune I.," Astrophys. J. 214, pp. 657-662.

Lockwood, G.W. (1978), "Analysis of Photometric Variations of Uranus and Neptune Since 1953," Icarus 35, pp. 79-92.

Pilcher, C.B. (1977), "Evidence for Weather on Neptune II.," Astrophys. J. 214, pp. 663-666.

Price, M.J. and Franz, O.G. (1976), "Limb Brightening on Uranus: The Visible Spectrum," Icarus 29, pp. 125-136.

Price, M.J. and Franz, O.G. (1978), "Limb Brightening on Uranus: The Visible Spectrum II.," Icarus 34, pp. 355-373.

Price, M.J. and Franz, O.G. (1979), "Uranus: Narrow-Waveband Disk Profiles in the Spectral Region 6000 to 8500 Angstroms," Icarus 38, pp. 267-287.

Trafton, L. (1974), "Neptune: Observations of the H_2 Quadrupole Lines in the (4-0) Band," in I.A.U. Symposium No. 65, "Exploration of the Planetary System," ed. A. Woszczyk and C. Iwaniszewska (Dordrecht: Reidel) pp. 497-512.

FIGURE CAPTIONS

Figure 1. Stellar Slit Scans (λ6800Å): Comparison of Calculation with Observation. Composite observational data are illustrated by the solid curve. The best-fitting analytical curve is illustrated by the broken curve. The slit width was 0.645 arc. sec. The sample interval was 0.032 arc. sec.

Figure 2. Stellar Slit Scans (λ7300Å): Comparison of Calculation with Observation. Composite observational data are illustrated by the solid curve. The best-fitting analytical curve is illustrated by the broken curve. The slit width was 0.645 arc. sec. The sample interval was 0.032 arc. sec.

Figure 3. Model Neptune Slit Scans. Theoretical Scans were computed for each of the six models listed in Table II. The Neptune disk was taken to be circularly symmetric with an apparent angular radius of 1.168 arc. sec. Atmospheric smearing was described by the mean point spread function discussed in the text. The slit width was 0.645 arc. sec. All slit scans were normalized to equal total energy, obtained by integrating over the disk of the planet. Broadening and flattening of the slit scans increases progressively with the degree of limb-brightening on the disk.

Figure 4. Neptune Slit Scans (λ6800Å): Comparison of Theory with Observation. Composite observational data are illustrated by the individual dots. The sample interval was 0.032 arc. sec. Theoretical scans, computed both for a uniform disk and for a ring of infinitesimal width, are illustrated by the solid curves. The Neptune disk was taken to be circularly symmetric with an apparent angular radius of 1.168 arc. sec. Atmospheric smearing was described by the relevant point spread function discussed in the text. The slit width was 0.645 arc. sec. All slit scans, both observational and theoretical, were normalized to equal total energy, obtained by integrating over the disk of the planet.

Figure 5. Neptune Slit Scans (λ7300Å): Comparison of Theory with Observation. Composite observational data are illustrated by the individual dots. The sample interval was 0.032 arc. sec. Theoretical scans, computed both for a uniform disk and for a ring of infinitesimal width, are illustrated by the solid curves. The Neptune disk was taken to be circularly symmetric with an apparent angular radius of 1.168 arc. sec. Atmospheric smearing was described by the relevant point spread function discussed in the text. The slit width was 0.645 arc. sec. All slit scans, both observational and theoretical, were normalized to equal total energy, obtained by integrating over the disk of the plant.

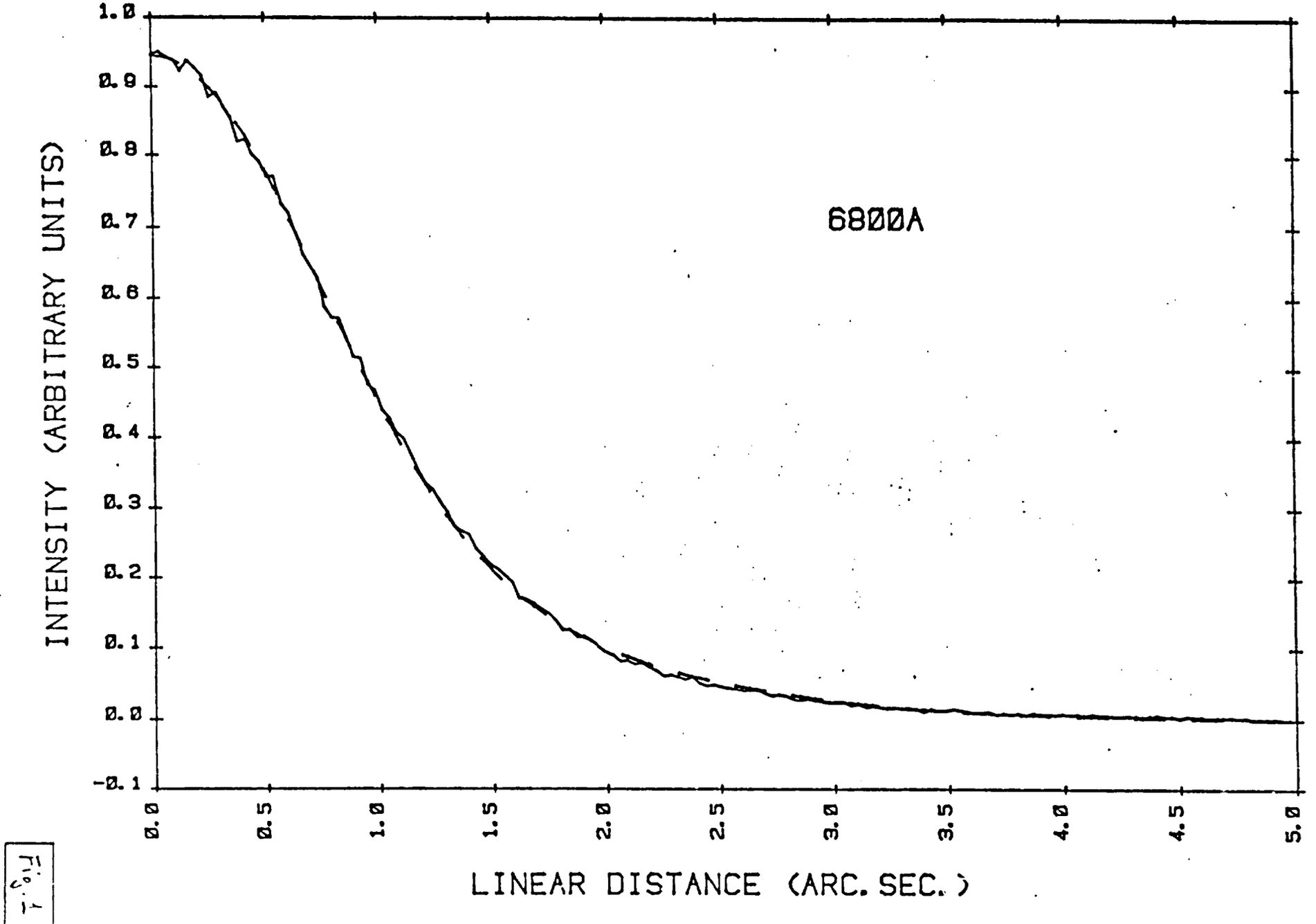
6800A
INTENSITY (ARBITRARY UNITS)
1.0
0.9
0.8
0.7
0.6
0.5
0.4
0.3
0.2
0.1
0.0
-0.1
0.0
0.5
1.0
1.5
2.0
2.5
3.0
3.5
4.0
4.5
5.0
LINEAR DISTANCE (ARC. SEC.)

FIG. 2

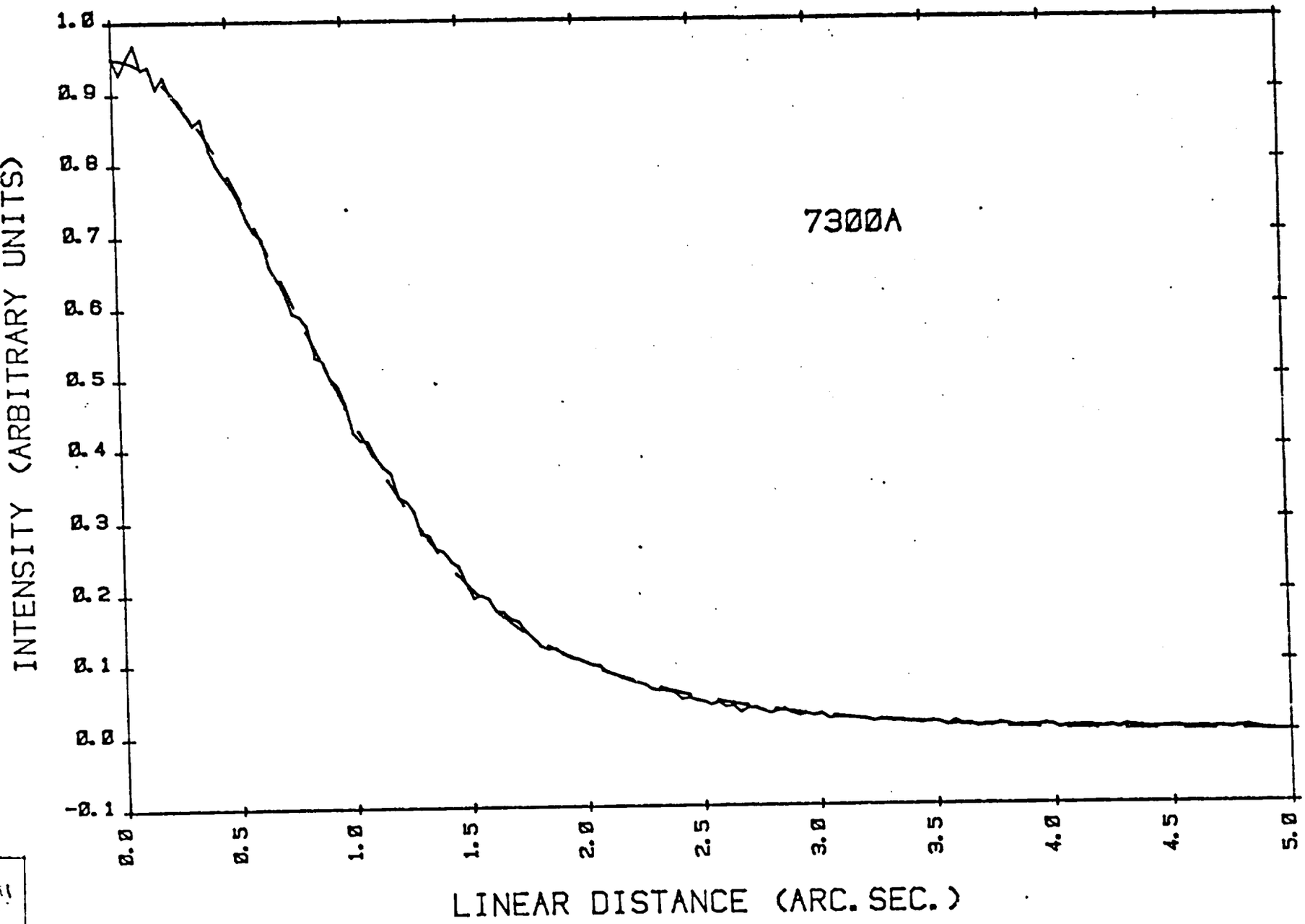
7300A
INTENSITY (ARBITRARY UNITS)
1.0
0.9
0.8
0.7
0.6
0.5
0.4
0.3
0.2
0.1
0.0
-0.1
0.0
0.5
1.0
1.5
2.0
2.5
3.0
3.5
4.0
4.5
5.0
LINEAR DISTANCE (ARC. SEC.)

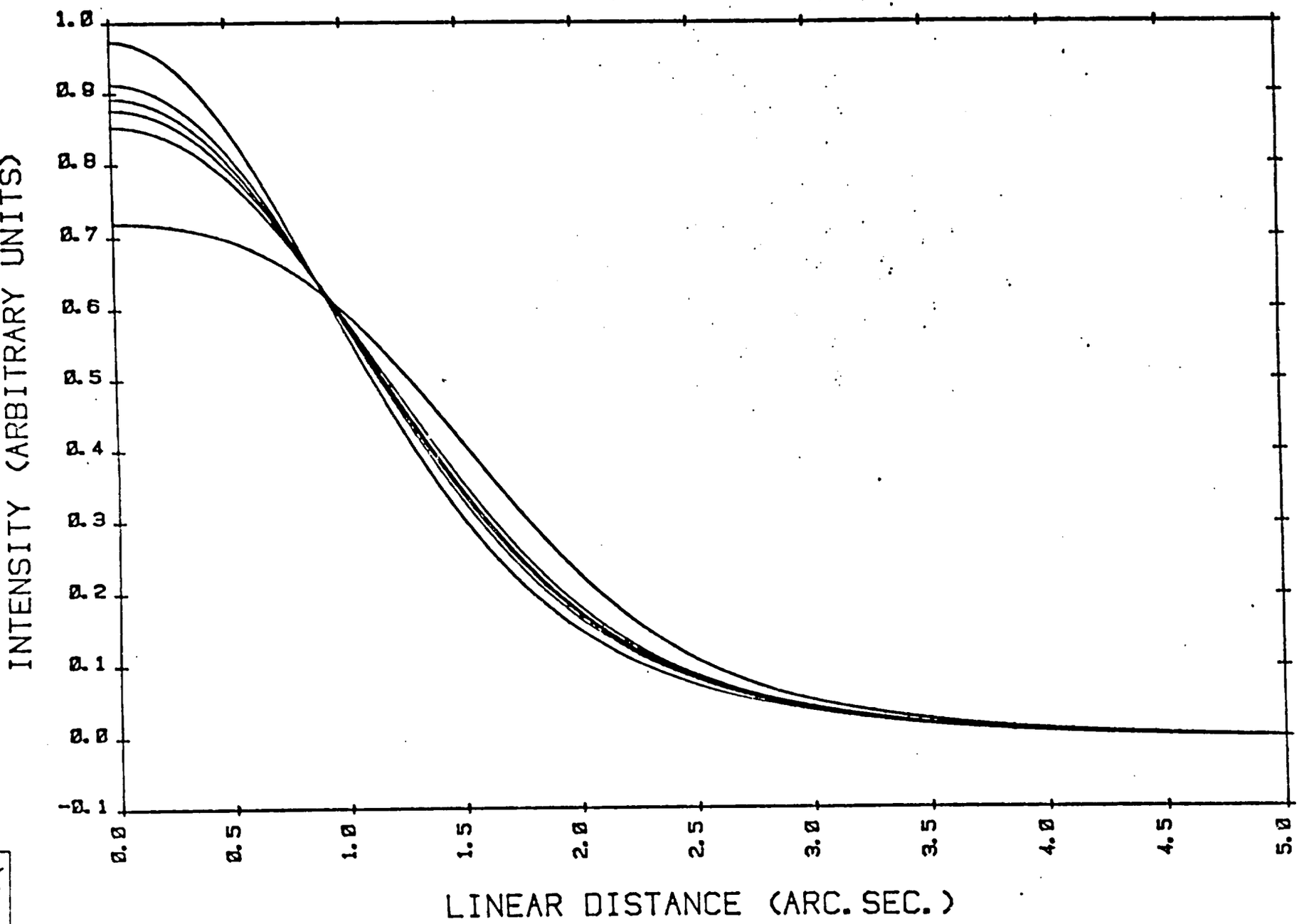
INTENSITY (ARBITRARY UNITS)
1.0
0.9
0.8
0.7
0.6
0.5
0.4
0.3
0.2
0.1
0.0
-0.1
0.0
0.5
1.0
1.5
2.0
2.5
3.0
3.5
4.0
4.5
5.0
LINEAR DISTANCE (ARC. SEC.)

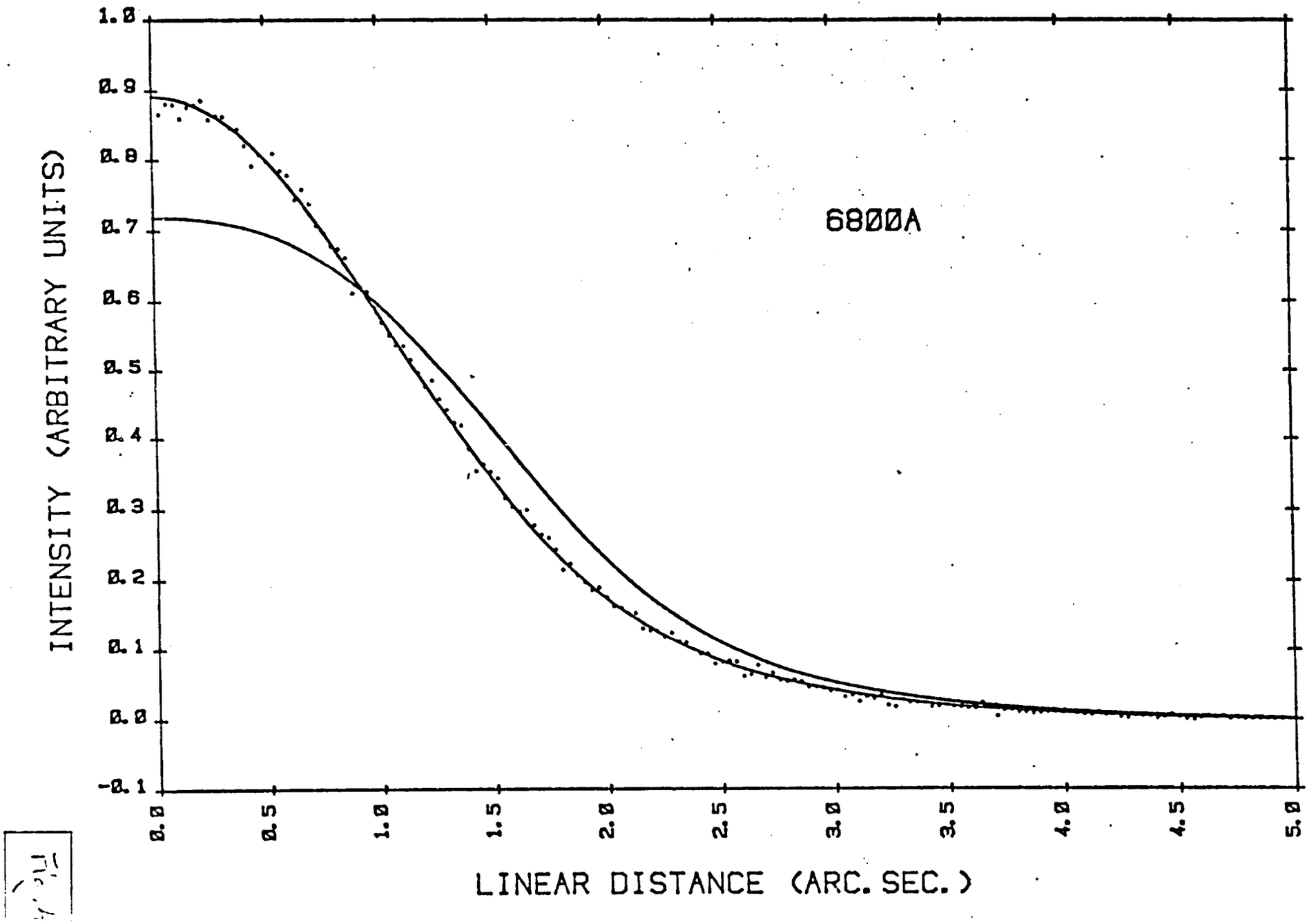
6800A
INTENSITY (ARBITRARY UNITS)
LINEAR DISTANCE (ARC. SEC.)
1.0
0.9
0.8
0.7
0.6
0.5
0.4
0.3
0.2
0.1
0.0
-0.1
0.0
0.5
1.0
1.5
2.0
2.5
3.0
3.5
4.0
4.5
5.0

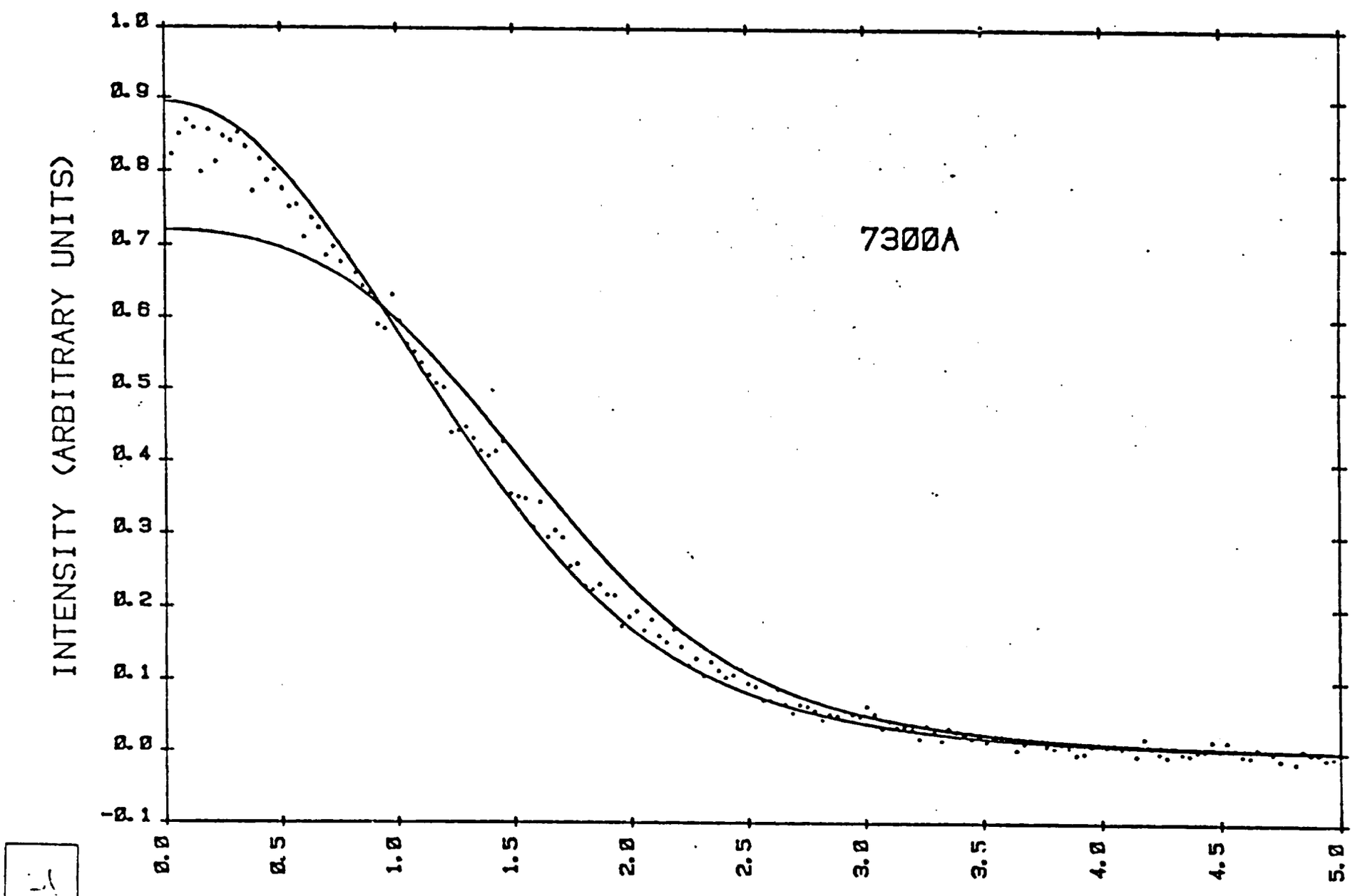
7300A
INTENSITY (ARBITRARY UNITS)
1.0
0.9
0.8
0.7
0.6
0.5
0.4
0.3
0.2
0.1
0.0
-0.1
0.0
0.5
1.0
1.5
2.0
2.5
3.0
3.5
4.0
4.5
5.0
LINEAR DISTANCE (ARC. SEC.)

APPENDIX D

NEPTUNE'S ROTATION PERIOD: A CORRECTION AND A SPECULATION ON THE EFFECT OF THE DISK BRIGHTNESS DISTRIBUTION

by

Michael J. S. Belton

L. Wallace

and

Sethanne H. Hayes

Kitt Peak National Observatory*

Tucson, Arizona

and

Michael J. Price

Science Applications, Inc.

Tucson, Arizona

Pages: 20

Tables: 2

Figures: 2

---

*Operated by the Association of Universities for Research in Astronomy, Inc., under contract with the National Science Foundation.

ABSTRACT

An error in the Hayes and Belton (1977) estimate of the rotation period of Neptune is corrected. If Neptune exhibits the same degree of limb darkening as Uranus near 4900 Å, the rotation period is 15.4 ±3 hours. This value is compatible with a recent spectroscopic determination of Munch and Hippelein (1979) who find a period of 11.2 $^{+1.8}_{-1.2}$ hours. However, if, as indirect evidence suggests, the law of darkening on Neptune at these wavelengths is less pronounced than on Uranus, then the above estimates may need to be lengthened by several hours.

Recent photometric data is independently analyzed and is found to admit several possible periods, none of which can be confidently assumed to be correct.

The period of Neptune most probably falls somewhere in the range 15 - 20 hours. The Hayes-Belton estimate of the period of Uranus is essentially unaffected by the above-mentioned error and remains at 24 ±4 hours. All observers agree that the rotation period of Uranus is longer than that of Neptune.

I. ERROR IDENTIFICATION

In a recent paper Munch and Hippelein (1979) have shown that the correction factors used by Hayes and Belton (1977) to remove the effects of atmospheric seeing from measurements of spectroscopic line tilts deviate strongly from analytical predictions. They find that this deviation systematically increases as the seeing conditions deteriorate. They suggested that a correct appraisal of the Hayes-Belton Neptune data should probably yield a period near 15 ±3 hours (rather than the published 22 ±4 hours) in agreement with their own independent measurement of $11.2\ ^{+1.8}_{-1.4}$ hours. The Hayes-Belton estimate of Uranus' period (24 ±3 hours) was not anticipated to be affected by this error, but they nevertheless note disagreement between this value and their own estimate of $15.0\ ^{+4.0}_{-2.6}$ hours.

We have re-examined the procedures by which the original Hayes-Belton seeing corrections were computed and have, in fact, located two serious sources of error. These are the failure to properly simulate the procedures by which the spectroscopic data was digitized, and a poor choice of integration limits in the seeing quadrature. The first of these errors leads to a systematically increasing underestimate of the magnitude of the seeing correction factor as the seeing conditions get worse. This is the behavior pointed out by Munch and Hippelein. The second error introduces "noise" into the seeing correction factors as a result of varying displacements of the pattern of quadrature points in the seeing algorithm with respect to the edge of the planetary disk.

These errors have been corrected and the original Hayes-Belton data re-analyzed. If we assume that the law of darkening on the two planets is identical to that derived by Danielson et al. (1972) from Stratoscope II observations of Uranus, we find the following values for the rotation periods of the two planets:

Uranus: 24.4 ±4 hours

Neptune: 15.4 ±3 hours

The conclusions of Hayes-Belton on the orientation of the polar axes and sense of spin of the two planets are unchanged. As an illustration of the correctness of the seeing algorithm, Figure 1 shows the agreement between seeing corrections evaluated by our program and those calculated by Munch and Hippelein. In this comparison we employ the same definition for the "center" of a spectroscopic line as was used by them. However, the actual correction factors used in the analysis depend on how the line center and tilt (cf. Hayes and Belton, 1977) of a line is defined in the data reduction process, and they are only roughly approximated (to about 6 percent of the correct value) by the analytical results in Figure 1.

II. DISCUSSION

(a) The Period of Neptune

Table I displays the most recent estimates of Neptune's rotation period and reveals a disturbingly wide range of values. The results reported in this paper are not only compatible with the rapid rotation found by Munch and Hippelein, but also with the much longer period of 18.44 hours favored by Slavsky and Smith (1978). The intercomparison of the latter two apparently mutually exclusive determinations is complicated by the existence of a possible period in the Slavsky and Smith data near 11 hours that was originally rejected by them on the grounds that this period produces an implausible light curve. This rejection is now known to have been premature and Smith and Slavsky (1979) report finding reasonable light curves for assumed periods near 10.42 hours and 18.44 hours.

The values of the dynamical and optical oblateness of the planet can in principle be used to discriminate between extreme values of the rotation period (cf. Hayes and Belton, 1977), however, in the case of Neptune even the best values of these parameters (Kovalevsky and Link, 1969; Freeman and Lynga, 1970) do not have sufficient accuracy. The optimum values of oblateness found by the above authors indicate a period near 14 hours, but the formal standard deviations are large enough to easily allow periods as short as 11 hours and as long as 18 hours.

In order to arrive at a position on the most likely value of Neptune's period, we have made an independent analysis of the

photometric data of Cruikshank (1978) and of Slavsky and Smith (1978). Also, we have reconsidered the assumptions underlying the spectroscopic estimates.

Photometric Periods: The most extensive data is that of Slavsky and Smith, and we have used two methods to find possible periods. The first is the Lafler-Kinman (1965) method in which a quantity θ is computed as a function of the assumed period. θ is the sum of the squares of the brightness differences between observations of adjacent phase, and we seek a minimum in its observed value by varying the assumed value of the period. This scheme selects periods which produce smooth light curves. The second method is closely related and was developed by L. Wallace. In this case θ is computed after the mean value of the brightness observations that fall within an assumed range of phase (we assumed intervals of 0.1 in phase) has been subtracted. This is analogous to a filtering process and serves to minimize high frequency variations, in the variable as a function of phase for an assumed period.

In their published work Slavsky and Smith use the full set of data, which extends over five lunations, to arrive at a period of 18.44 hours. The data was, however, "corrected" by removing the mean value and trend from the data taken at the separate lunations, justifying this operation by changes in the reference stars that were used and photometric "weather on Neptune. In the near infrared the latter is known to show dramatic changes on a monthly time scale (Joyce et al., 1977) and could lead to both amplitude modulation of the photometric signal and also phase

shifts between one lunation and the next. The results of such variability, especially when combined with aliasing by the sampling spectrum, could lead to the presence in the data of many possible light curves, each characterized by similar scatter, but which correspond to spurious periods. As a result there is, in our opinion, no *a priori* guarantee that even the best looking curve will correspond to the true period. A Fourier analysis of the brightness-time data would give an equivalent view with many peaks showing up in the power spectrum well above the background noise set by the photometric accuracy of the data (cf. Fig. 6 in Slavsky and Smith, 1978).

In our analysis we have attempted to minimize the above problems by analyzing individual lunations in Slavsky and Smith's and Cruikshank's data separately and have not applied any *ad hoc* corrections to the listed data. However, we have also analyzed the full data set in order to provide a direct comparison to Slavsky and Smith. [We note that the photometric quantity R_p/R_* would have been preferred to the quantity $R_p - R_*$ which Slavsky and Smith used in their analysis; however, they only list the latter quantity. The use of the ratio would, we believe, more effectively assure the removal of any changes in instrumental response that might occur from night to night.] Our results are collected in Table II and in Figure 2. In the case of Cruikshank's data, we have omitted from consideration the five data points associated with the May-June, 1977 time period in order to keep the data restricted to single lunation.

We conclude from a comparison of the various data that there is little reason to accept 18.44 hours as a secure identification

of the planetary period. This period is certainly not predominant in the monthly solutions, although periods near to this value do produce reasonable light curves for all except the March-April 1977 Slavsky-Smith data. From the data plotted in Figure 2 we conclude that any of the listed periods based on the full data set are acceptable. Finally, in comparing the Cruikshank and Slavsky-Smith data for July 1977, we notice that a period of 21.03 hours seems to provide a reasonably low scatter light curve for both sets of data and a rough comparison of trends in the two sets of data during the few days (July 10-14, 1977) where they are in common, shows strong similarities in the behavior of the $R_p - R_*$ and J - K indexes with time; the significance of this, however, is far from clear.

Spectroscopic Periods: Underlying the determination of spectroscopic periods reported here is the assumption that the degree of limb darkening exhibited by Neptune is identical to that of Uranus (at least near 4900 - 5000 Å where the measurements are made). If, however, the limb darkening on Neptune is, in fact, less pronounced than has been assumed, then the true period will be longer than the current estimates. For example, if Neptune has a flat distribution of light across its disk at 4900 Å, then the Hayes-Belton data would imply a period some six hours longer ($\sim$ 21 hours) than the value noted in Section I.

Contrary to the position taken by Hayes and Belton in 1977 we note that there now exists a recent and growing body of indirect evidence for significant differences in the atmospheres of the two planets which could, we speculate, be indicators of

a substantial difference in their limb darkening properties. For example, the higher albedo shown by Neptune in the center of strong CH_4 bands (Wamsteker, 1973), the different shape of strong methane bands in the 1 - 2.5μ region (Fink and Larson, 1979), and the greater photometric variability of Neptune relative to Uranus (Slavsky and Smith, 1978; Avis et al., 1977; Lockwood, 1978) all could be indicators of a substantial and global presence of aerosols high in Neptune's atmosphere that is largely absent on Uranus. On the other hand this aerosol component (should it exist) is nevertheless constrained to be optically thin in order that the similarity of hydrogen quadrupole spectrum between the two planets can be reasonably understood (Trafton, 1974). A coupling of this admittedly speculative evidence for a thin (but, relative to Uranus, substantial) scattering haze high in Neptune's atmosphere together with the indication in Wamsteker's (1973) work that Neptune's geometric albedo is less than that of Uranus in the region 4000 - 5200 Å, leads to the possibility that Neptune's limb darkening might be substantially reduced from that exhibited by Uranus. We also note that recent measurements of the distribution of brightness across Neptune's disk in the "continuum" near 6800 Å by Price and Franz (1979a) indicate that model brightness distributions that are flat or marginally limb brightened are required to best explain the data. Similar "continuum" observations of Uranus at 6200, 6400, and 7500 Å, on the other hand, all indicate the presence of some limb darkening (Price and Franz, 1979b). While such observations do not definitely prove the speculations made regarding the relative limb

darkening on the two planets (e.g., no similar brightness distribution scans exist for Uranus and Neptune at exactly the same wavelengths that the rotation studies were done), they do nevertheless seem to indicate that there is a reasonable chance of their being correct. Thus, we argue that there is a substantial possibility that the spectroscopic periods estimated for Neptune by Munch and Hippelein (1979) and by us are too short by several hours.

In conclusion it is our assessment that the period of Neptune is most likely to be longer by several hours than the current spectroscopic estimates of 11.2 to 15.4 hours. The exact value is unknown and is not necessarily one of the values indicated by current observations of its brightness variation. Many more occultation chords, which could help tie down the oblateness more accurately, are needed as are much more densely sampled light curves. Imaging of the planet in regions of CH_4 absorption may, however, ultimately yield the most accurate estimate of the period (Reitsema, private communication).

(b) The Period of Uranus

Current estimates of the rotational period of Uranus depend only on the spectroscopic technique and estimates of the planet's oblateness. Its brightness is apparently not appreciably modulated by rotation (Lockwood and Thompson, 1978; Avis et al., 1977, cf. Hayes and Belton (1977) for earlier photometric references) and so no modern light curves have yet been published. Estimates of the planet's oblateness vary from 0.01 ±0.01 (Danielson et al.,

1972) to the most recent value of 0.033 ±0.007 which was obtained from observations of a stellar occultation by the planet (Elliot et al., 1979). Because of this spread oblateness is not, in our opinion, a predictor of the rotation period that can be used with confidence. The spread of values relative to the formal errors indicate that strong systematic errors may affect one or more of the various determinations. The estimate of oblateness which has the smallest *formal* error is that of Franklin et al. (1978) who find a value of 0.021 ±0.001 based on a careful reanalysis of the stratoscope images (Danielson et al., 1972). This value leads to a highly constrained period of 16.8 ±0.8 hours which would exclude the period found by Hayes and Belton (1977) if the possibility of systematic errors is ignored and the formal error in the determination of the oblateness is taken at face value. We, however, prefer to interpret the range of oblateness determinations as indicative of the magnitude of systematic errors that can occur in the various determinations of this quantity and use the oblateness as a discriminator rather than a predictor. We note that the period of 24 ±4 hours yields an oblateness in the range 0.011 and 0.016 and that this range of values falls between the results of Elliot et al. on the one hand, and Danielson et al. on the other; this estimate is, therefore, a reasonably probable value for the period if current determinations of oblateness are to be used as a criteri .

We conclude that it is not possible at present to choose confidently between the Trafton/Hayes-Belton period (∿ 24 hours) on one hand and the Trauger et al./Munch-Hippelein/Brown-Goody

periods ($\lesssim$ 16 hours) on the other and that any of these estimates may be close to the actual period. However, we note that the Hayes-Belton data on Uranus and Neptune were obtained at the same observing sessions, under identical instrumental conditions, and reduced in an identical fashion; it, therefore, seems reasonable to make the following statements: The period of Uranus is longer than that of Neptune, and that if the Hayes-Belton estimate of Neptune's period is proved correct, then so, probably, is their estimate of the period of Uranus.

ACKNOWLEDGMENTS

We are very grateful to Dr. G. Munch and Dr. H. Hippelein and to Dr. F. A. Franklin for communicating their results to us prior to publication.

REFERENCES

Avis, C. A., Smith, H. J., Bergstrahl, J. R., and Sandman, W. H. (1977). "Photometric Determination of the Rotation Period of Uranus" *Bull. A.A.S.*, 9, 472.

Brown, R. A., and Goody, R. M. (1977). "The Rotation of Uranus" *Astrophys. J.*, 217, 680.

Brown, R. A., and Goody, R. M. (1979). "The Rotation of Uranus II" *Astrophys. J.*, in press.

Cruikshank, D. P. (1978). "On the Rotation Period of Neptune" *Astrophys. J. Letters*, 220, L57.

Danielson, R. E., Tomasko, M. G., and Savage, B. D. (1972). "High Resolution Imagery of Uranus Obtained by Stratoscope II" *Astrophys. J.*, 178, 887.

Elliot, J. L., Dunham, E., Mink, D. J., Churms, J. (1979). "The Radius and E-lipticity of Uranus from Its Occultation of SAO 158687" *Astrophys. J. Letters*, submitted for publication.

Fink, U., and Larson, H. P. (1979). "The Infrared Spectra of Uranus, Neptune, and Titan from 0.8 to 2.5 Microns" *Astrophys. J.*, in press.

Franklin, F. A., Avis, C. C., Colombo, F., and Shapiro, I. I. (1979). "The Geometric Oblateness of Uranus" preprint, submitted to *Astrophys. J.*

Freeman, R., and Lynga, G. (1970). "Data for Neptune from Occultation Observations" *Astrophys. J.*, 160, 767.

Hayes, S. H., and Belton, M. J. S. (1977). "The Rotational Periods of Uranus and Neptune" *Icarus*, 32, 383.

Joyce, R. R., Pilcher, C. B., Cruikshank, D. P., and Morrison, D. (1977). "Evidence for Weather on Neptune. I" *Astrophys. J.*, 214, 657.

Kovalevsky, J., and Link, F. (1969) "Diamétre, aplatissement et Propriétes optiques de la haute atmosphère de Neptune d'apres l'occultation de l'etoile BD - 17°4388" *Astron. and Astrophys.*, 2, 398.

Lafler, T., and Kinman, T. D. (1965). "An RR Lyrae Star Survey with the Lick 20 Inch Astrograph" *Astrophys. J. Suppl.*, 11, 216.

Lockwood, G. W., and Thompson, D. T. (1978). "A Photometric Test of Rotation Periods for Uranus and Time Variations of Methane Band Strengths" *Astrophys. J.*, 221, 689.

Lockwood, G. W. (1978). "Analysis of Photometric Variation of Uranus and Neptune Since 1953" *Icarus*, 35, 79.

Munch, G., and Hippelein, H. (1979). "The Effects of Seeing on the Reflected Spectrum of Uranus and Neptune" submitted to *Astron. and Astrophys. (Main Journal)*.

Nicholson, P. D., Persson, S. E., Mathews, K., Goldreich, P., and Neugebauer, G. (1978). *Astron. Journal*, 83, 1240.

Price, M. J., and Franz, O. G. (1979a). "Neptune: Limb Brightening Within the 7300 Angstrom Methane Band" in course of publication.

Price, M. J., and Franz, O. B. (1979b). "Uranus: Narrow-Waveband Disk Profiles in the Spectral Region 6000 to 8500 Angstroms" *Icarus*, 38, 267.

Smith, H. J., and Slavsky, D. (1979). Private communication.

Slavsky, D., and Smith, H. J. (1978). "The Rotation Period of Neptune" *Astrophys. J. Letters*, 226, L49.

Trafton, L. (1974). "Neptune: Observations of the H_2 Quadrupole Lines in the (4-0) Band" in "Exploration of the Planetary System" ed. A. Woszczyk and C. Iwaniszerska. I.A.U. Symposium No. 65. D. Reidel Co.

Trafton, L. (1977). "Uranus' Rotation Period" *Icarus*, 32, 402.

Trauger, J. R., Roesler, F. L., and Munch, G. (1978). " A Redetermination of the Uranus Rotation Period" *Astrophys. J.*, 219, 1079.

Wamsteker, W. (1973). "The Wavelength Dependence of the Albedos of Uranus and Neptune from 0.3 to 1.1 Microns" *Astrophys. J.*, 184, 1007.

TABLE I.

Recent Spectroscopic and Photometric Estimates of the Rotational Periods of Neptune and Uranus

Source	Period (Hours)
a) Neptune	
1. This paper	15.4 ±3
2. Munch & Hippelein (1979)	11.2 $^{+1.8}_{-1.2}$
3. Slavsky & Smith (1978)	18.44 ±0.01
4. Cruikshank (1978)	19.53 ±0.05 18.17 ±0.05
b) Uranus	
1. Hayes & Belton (1977)	24 ±3
2. Munch & Hippelein (1979)	15.0 $^{+4.0}_{-2.6}$
3. Brown & Goody (1979)	16.16 ±0.33
4. Trauger, Roesler & Munch (1978)	13.0 ±1.3
5. Trafton (1977): Method I	>15.4
Method II	23 $^{+5}_{-2}$

TABLE II.

Possible Photometric Periods (in hours)

CRUIKSHANK (1978)		SLAVSKY and SMITH (1978)									
July, 1977		FULL DATA SET		March-April 1977		June 1977		July 1977		August 1977	
Period	Θ	Period	Θ*	Period	Θ	Period	Θ	Period	Θ	Period	Θ
19.39	0.7498	18.45	0.02095	16.30	0.4046	18.42	0.3587	21.03	0.7539	18.99	0.6817
18.15	0.7870	19.16	0.02314	9.67	0.4226	12.84	0.4687	18.85	0.8616	21.03	0.7086
21.03	0.9573	19.06	0.02343	19.36	0.4639	17.11	0.8189	13.45	0.8738	10.45	0.7152
14.81	0.9690	10.42	0.02414	18.37	0.7549	10.27	0.8195	8.87	0.9176	20.31	0.7450
10.34	1.1151	15.25	0.02429	15.56	0.9117	13.20	0.8786	21.82	1.0299	13.01	0.8350

*The analysis of the full data set was based on L. Wallace's modification of the Lafler-Kinman technique (see text).

FIGURE CAPTIONS

Fig. 1. Comparison of seeing correction factors computed by Munch and Hippelein (1979) and those computed by the corrected Hayes-Belton program. In this figure MH refers to Munch-Hippelein and BG to Brown-Goody(1977). σ is the seeing parameter and $M_1(r)$ is the mean displacement of a spectral line measured at a distance r from the center of the disk. In this graph the line displacement at the limb is normalized to r and the seeing parameter is normalized to the planetary radius [cf. Munch and Hippelein(1979)].

Fig. 2. Light curves deduced from the data of Slavsky and Smith (1978) for four assumed periods. The period of 18.44 is preferred by Slavsky and Smith. In this paper we conclude that the qualitative differences in the various light curves are so small that all of the plotted periods are equally acceptable.

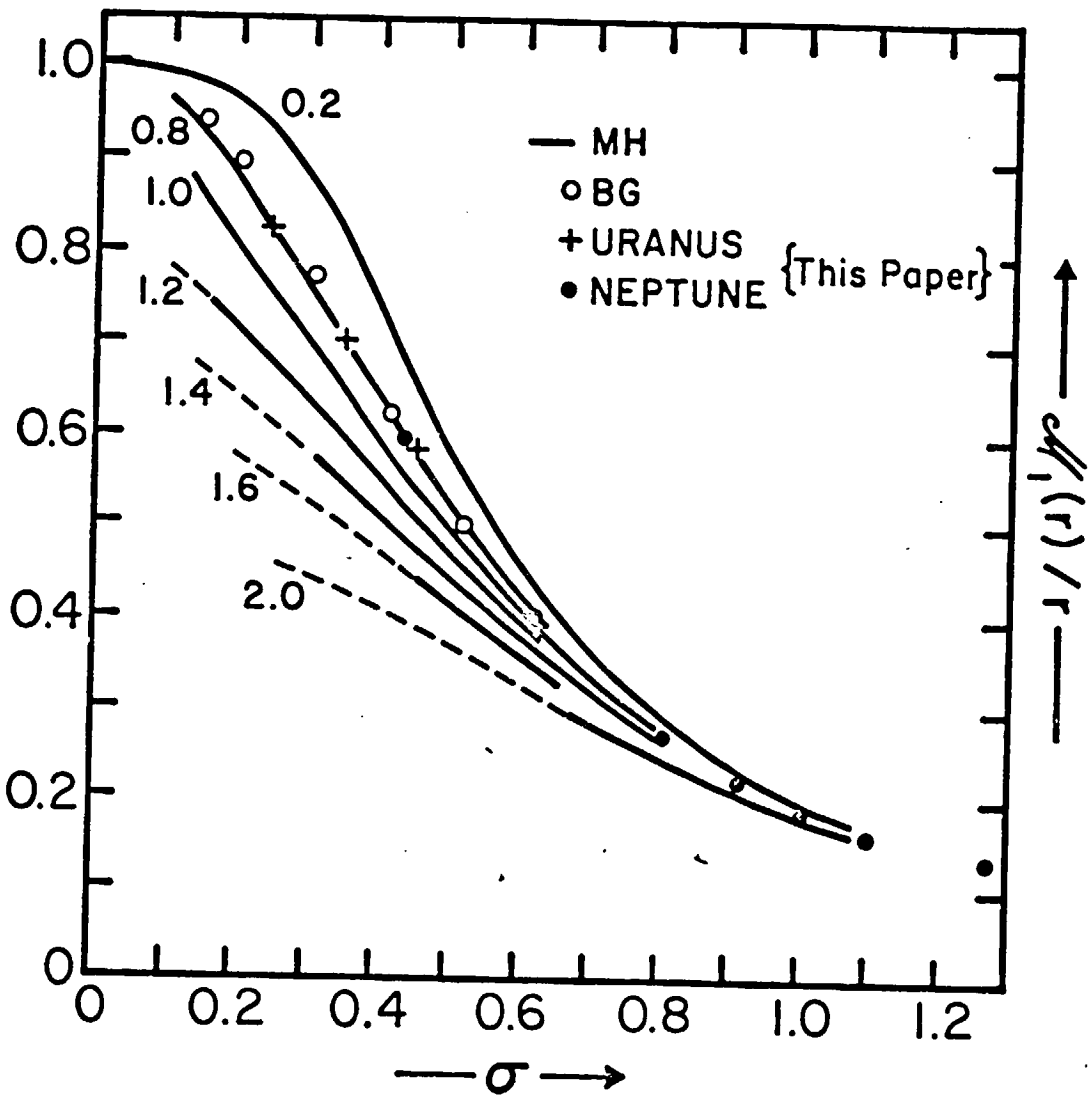
1.0
0.8
0.6
0.4
0.2
0
0
0.2
0.4
0.6
0.8
1.0
1.2
σ
0.2
0.8
1.0
1.2
1.4
1.6
2.0
MH
BG
URANUS
NEPTUNE
{This Paper}
ω'(r) / r

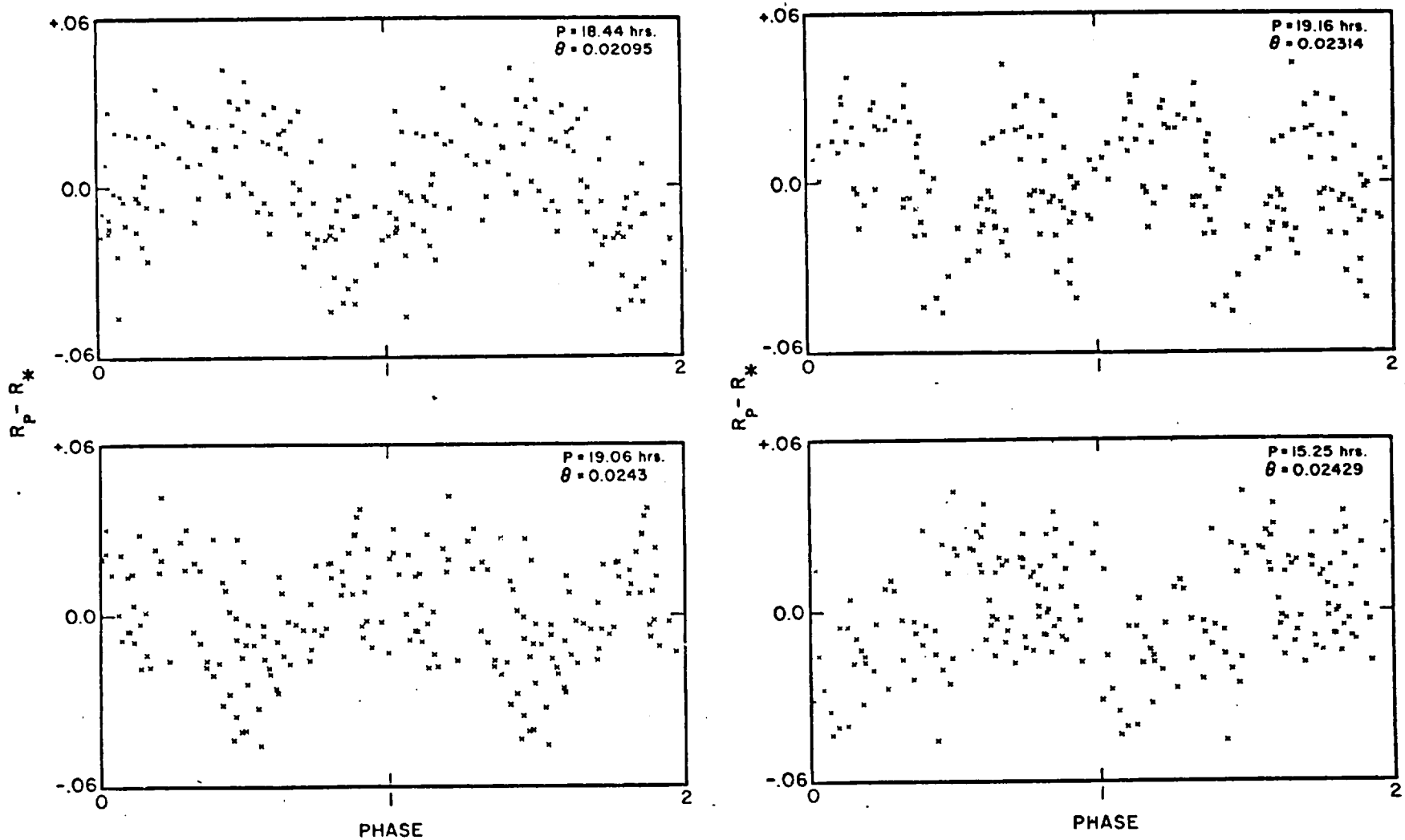
P = 18.44 hrs.
θ = 0.02095
P = 19.16 hrs.
θ = 0.02314
P = 19.06 hrs.
θ = 0.0243
P = 15.25 hrs.
θ = 0.02429
+.06
0.0
-.06
0
1
2
$R_p - R_*$
PHASE

APPENDIX E: "Observing Report on 1979 Activities at Kitt Peak National Observatory"

Submitted by Donald R. Davis

OBSERVING REPORT ON 1979 ACTIVITIES AT KITT PEAK NATIONAL OBSERVATORY

1. Infrared Search for Small Bodies in the Inner Solar System

This project is a daytime search for small bodies hypothesized to orbit the Sun interior to Mercury's orbit. The IR search at 3.5μ and 4.6μ capitalizes on the fact that the signal from such objects is significantly enhanced by thermal emission due to their high surface temperatures. The search technique is to scan small regions of the sky from 8^{o} to 15^{o} from the Sun and within 1^{o} of the ecliptic plane. If a detection is found, the coordinates are noted, and the same area is rescanned later to see if the detection recurs at the same location. If so, it is assumed to be a natural object, otherwise a new search is undertaken to recover the detection. A hexcel baffle mounted on the open end of the 1.3m telescope collimates the sunlight so that we can point as close as 5^{o} from the Sun without having sunlight falling directly onto the mirror. The major unresolved problem from our 1978 exploratory run, namely that of accurately repointing the telescope to the point where a detection was found in the scan mode, was corrected by precisely rebalancing the telescope with the baffle mounted. During 1979, about 5 days were devoted primarily to scanning with the rest being lost to bad weather or instrument/computer problems and system set-up and experimentation. During this time, we scanned 2.5 square degrees within the search area without any detections having the characteristics expected for orbiting intra-Mercurial objects. Based on our estimated detection limit of ∿50 km and plausible population distributions, we estimate there would be ∿25% chance of having found them during this search. Covering an area larger by a factor of ∿3, which we hope to accomplish next year, should allow us to establish more definitive limits on this hypothesized population. An abstract of phases of this work may be found in Bull.A.A.S., 11, No. 3, 553 (1979).

2. Infrared Radiometry of Asteroids

A program to obtain radiometric measurements at 5μ, 10μ, and 20μ was undertaken to take advantage of the fact that the 1.3m telescope was not scheduled some nights during our daytime search run. These observations allow asteroid albedos and diameters to be determined and, when combined with other spectrophotometric data, permit a more thorough investigation of asteroid surface properties. Data were obtained on 20 asteroids during April, 1979. Preliminary reductions suggest the following asteroids have low albedos: 6, 52, 268, 419, 554, 624, 638, and 1323; the following have relatively high albedos: 5, 7, 15, 22, 62, 92, 349, and 727; a few have intermediate albedos: 8, 40, 130, and 379. Final data reduction and paper preparation are currently in progress.

Donald R. Davis

Donald R. Davis
Planetary Science Institute
2030 East Speedway, #201
Tucson, Arizona 85719

APPENDIX F

DYNAMICAL EVOLUTION OF INTRA-MERCURIAN PLANETESIMALS

Donald R. Davis
Stuart J. Weidenschilling

Planetary Science Institute
2030 East Speedway
Tucson, Arizona 85719

The existence of bodies orbiting interior to Mercury is a subject that has received considerable attention in the past, particularly in the first two decades of this century, when interest was stimulated by an unexplained component in the precession of Mercury's perihelion. One hypothesis to explain the anomalous precession was gravitational perturbations due to the presence of a yet undetected body orbiting between Mercury and the Sun. Photographic searches during total solar eclipses carried out by Perrine (1902, 1906, 1909), and Campbell and Trumpler (1923) failed to detect any object down to a diameter larger than 100 km, hence they concluded that any intra-Mercurial bodies must be small, faint objects. More recently, Courten (1976) searched for faint objects near the Sun using solar eclipse photography. Preliminary reports of detection of small objects located within 20 solar radii of the Sun have yet to be independently confirmed. The area covered and published magnitude limit of searches carried out to date are summarized in Figure 1. An object 60 km in diameter would have a visual magnitude of 8.0 at a distance of 0.28 A.U., corresponding to an 18° maximum elongation, assuming the same albedo as the mean of the first four asteroids (0.13). With Mercury's albedo of 0.07, the corresponding size is 82 km. Previous searches have shown that there are no bodies larger than 50-100 km diameter orbiting interior to Mercury's orbit; however, these searches do not preclude the existence of smaller bodies.

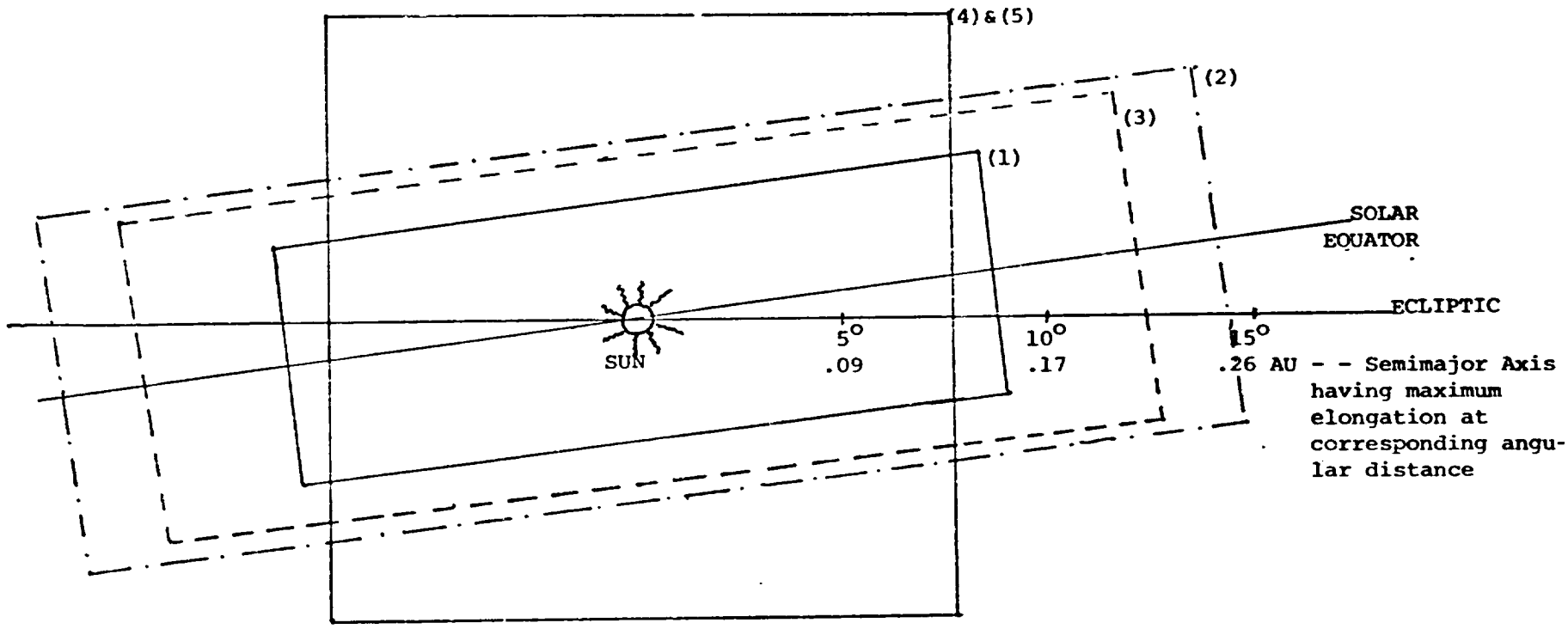

FIGURE 1: SEARCH REGION AND LIMITING PHOTOGRAPHIC MAGNITUDE FOR PREVIOUS SOLAR ECLIPSE PHOTOGRAPHIC SEARCHES

The failure of searches in the early part of this century to find intra-Mercurial objects effectively dampened enthusiasm for further investigation. However, there has been further exploration of this region in connection with the occurrence of Sun-grazing comets. Photographic searches during solar eclipses from 1963-1973 were primarily motivated by cometary investigations; however, indications of several non-stellar images again suggested the possibility of small objects orbiting close to the Sun.

Theoretical justification for the possible existence of intra-Mercurial objects was recently supplied by Weidenschilling (1978), who proposed an aerodynamic fractionation model to explain the low mass and high Fe content of Mercury. This model suggests that nebular gas drag, causing planetsimals to spiral inward from the region of Mercury, could have removed a large fraction of an Earth mass from Mercury's zone. Most of this matter spiraled into the Sun, however, as the nebular gas dispersed and the drag ceased, as much as $\sim 5 \times 10^{-3}$ $M_{\oplus}$ could have remained in orbit inside of Mercury's orbit. Even if no significant mass condensed directly from the solar nebulas in this region, as suggested by equilibrium condensation models of Lewis (1972), aerodynamic fractionation could have transported matter inward from the larger distance where it did condense. The discovery of intra-Mercurial bodies could be strong evidence supporting the aerodynamic fractionation model.

If such bodies existed in the earliest epoch of solar system history, could they survive to the present day, and, if so, where

would they be located and could they be detected? Following dispersal of the dissipative medium, collisions are the dominant mechanism for determining subsequent evolution. We suggest that the population consisted of a size-distribution containing $\sim 5 \times 10^{-3}$ $M_\odot$ moving on low eccentricity, low inclination orbits (due to damping by the gas) approximately uniformly distributed in semimajor axis $\underline{a}$.

The most important factor in determining the outcome of collisions is the speed at which the bodies collide, which is governed by the orbits on which the bodies move. After dispersal of nebular gas, planetary gravitational perturbations will begin to stir up orbital eccentricities and inclinations. The large amplitude, long period variations, the so-called secular perturbations, are the most important component of orbital changes. Secular perturbations in both Mercury's orbit and planetesimal orbits cause some bodies to become partial Mercury crossers, which will be eliminated by imacting on Mercury. The orbital variation of an initial low eccentricity, low inclination orbit due to secular perturbations, as well as the variation in Mercury's perihelion distance is illustrated in Figure 2. The initial orbit has $\underline{a}$ = 0.25 A.U. and a small initial eccentricity (e = .001); however, planetary perturbations drive the orbit to being just Mercury crossing for a small fraction of the time. While the orbits overlap, there exists a chance the orbits will actually intersect and that impacts onto Mercury may occur; hence bodies on this or adjacent orbits will be eliminated by Mercury impacts, although possibly on a long

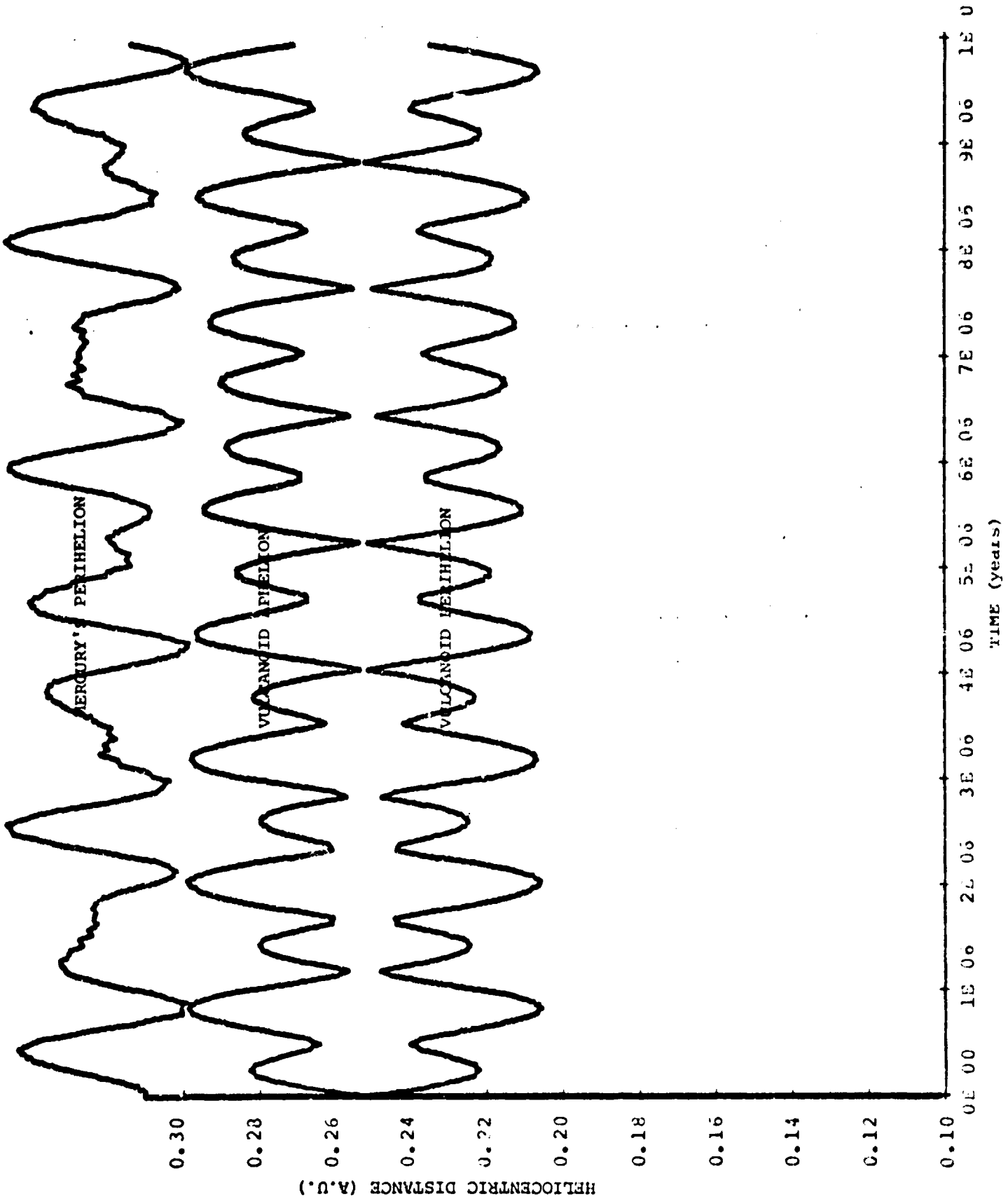

FIGURE 2: HELIOCENTRIC DISTANCE VARIATIONS DUE TO SECULAR PERTURBATIONS ON AN INITIALLY NEARLY CIRCULAR ORBIT WITH $\underline{a}$ = 0.25 A.U. ALSO SHOWN IS THE VARIATION IN MERCURY'S PERIHELION DISTANCE DUE TO PLANETARY PERTURBATIONS ON MERCURY.

timescale, since collisions are possible only a small fraction of the time. Similar orbits but having $\underline{a}$ > 0.25 A.U. will be even deeper Mercury-crossers and would be eliminated on average, even more rapidly; hence any obdy initially moving on an orbit with $\underline{a}$ > 0.25 A.U. (with the possible exception of certain commensurability cases) will be eliminated by Mercury impacts. This population could contribute a long-lived tail to the post-accretion Mercury impact flux; quantitative calculations of this component are currently underway.

Bodies on orbit with $\underline{a}$ < 0.25 A.U. could be eliminated by Mercury impacts provided the free eccentricity is sufficiently large; however, due to gas drag that would damp eccentricities, it is expected that free eccentricities would be small. The maximum forced eccentricity for bodies on nearly circular orbits with $\underline{a}$ < 0.25 A.U. is shown in Figure 3 to be a generally decreasing function with decreasing $\underline{a}$, except for the spike near $\underline{a}$ = 0.23 A.U., which arise due to a secular resonance between the orbital periapse rate and the characteristic precession rate of Uranus. Similar variations are found for inclination perturbations. The question now remains as to how variations in eccentricity and inclinations translate into changes in mean collision speeds. The bodies that collisionally interact are those that have similar $\underline{a}$'s, and hence have similar forced variations in e and i. Hence, the phased variations violate the assumption of random orbits that is the basis for calculating mean impact speed by Safronov (1969) and Greenberg et al. (1978). However,

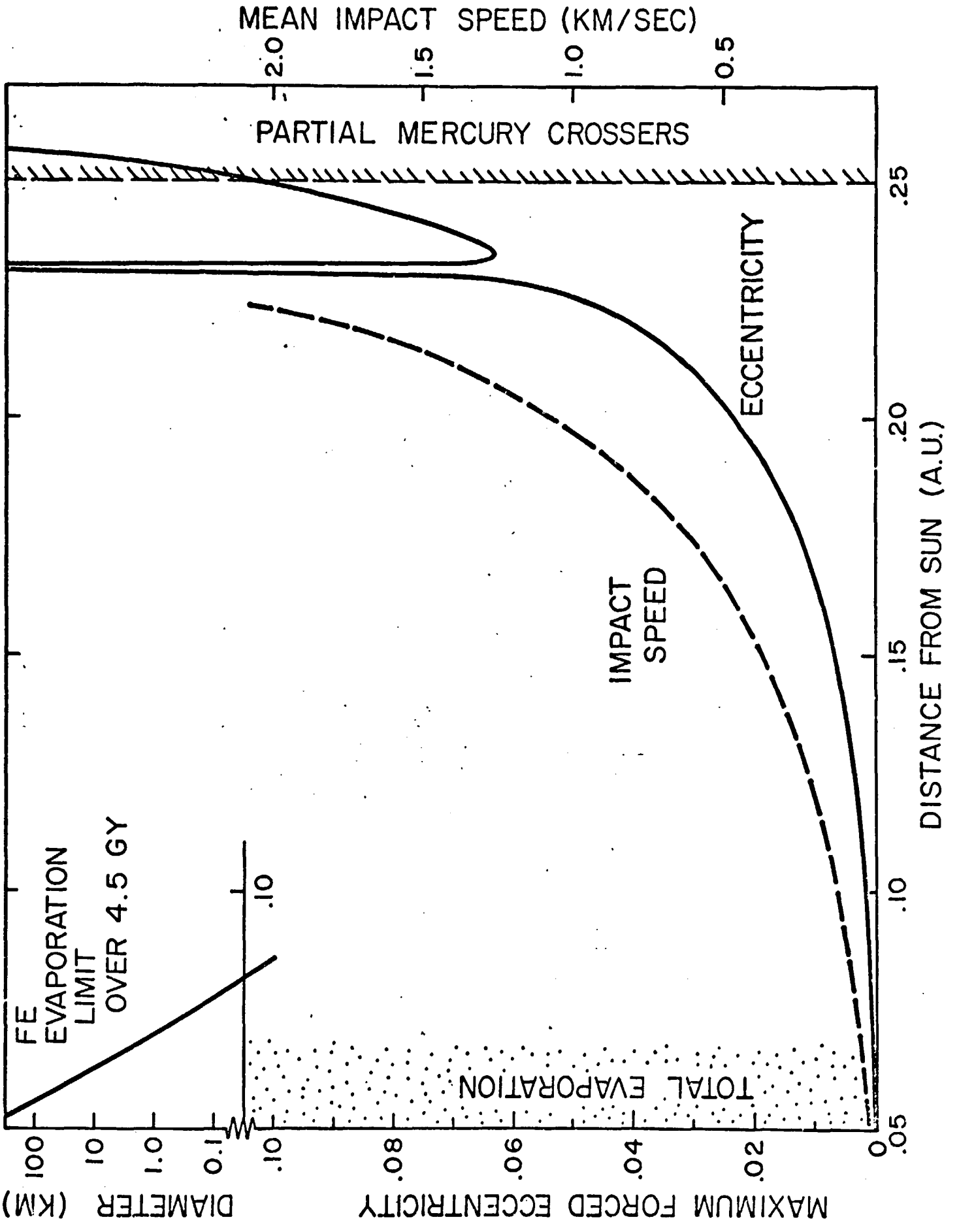

FIGURE 3. MAXIMUM FORCED ECCENTRICITY AND MEAN IMPACT SPEED AS A FUNCTION OF SEMIMAJOR AXIS.

there are collisions occurring among the particles which will reduce orbital phasing and so long as collisions are frequent on the timescale of orbital variations, the assumption of orbital randomness is a good approximation. The average collision speed given in Figure 3 is found using mean eccentricities and inclinations as a function of a in the equations of Greenberg *et al.* (1978). Using this methodology, the mean impact speed varies from $\sim$3 km/sec near a = 0.25 A.U. down to less than 100 m/sec at 0.05 A.U.

An upper bound on the semimajor axis of stable orbits interior to Mercury was shown to be 0.25 A.U. A minimum distance for possible survivability over the age of the solar system can be estimated based on the sublimation rate for various materials. At small a, vulcanoid temperatures will be quite high and if the object is close enough to the Sun, there will be appreciable mass loss due to evaporation. Using an approach similar to that of Lebofsky (1975), we estimate the size of Fe objects that would totally evaporate over the age of the solar system as a function of orbital a in Figure 3. The evaporation rate is a strong function of a and effectively precludes survival of bodies which were initially several tens of kilometers in size within $a \tilde{=}$ 0.07 A.U. Conceivably, other materials could survive inside this limit if they have lower vapor pressures; however, given the steep temperature rise with decreasing distance, it is difficult to imagine that bodies could survive very much closer than than $a \gtrsim$ 0.07 A.U., unless they were very large bodies initially.

For the initial size bodies we consider, we adopt 0.07 A.U. as the lower bound on a for survivability.

Bodies that initially formed or were transported into the zone from 0.07 to 0.25 A.U. would be removed primarily by collisional depletion. The collisional evolution program developed to explore asteroid and planetesimal evolution (Davis et al., 1979; Greenberg et al., 1978) was adapted to study the collisional evolution of vulcanoids over the age of the solar system. The main alteration to the existing program was to include effects of secular perturbations on mean collision speeds. This was implemented by adding a term for the rate of change of mean impact speed due to secular perturbations to the algorithm for calculating the total velocity change during a time step. Various initial conditions were input to the model and subsequent evolution over the 4.5 Gy age of the solar system traced. The program is currently capable of modeling a region of the solar system for which a single mean impact speed can be used over all heliocentric distances; and as indicated in Figure 3, there is a rapid change in mean collision speed from 0.07 to 0.25 A.U. In order to match this and other assumptions implicit in the numerical model, narrow semimajor axis zones were used to determine the overall evolution of objects initially located between 0.07 and 0.25 A.U. Nominal input parameters for these collisional evolution runs are given in Table 1.

Evolution outcomes after 4.5 Gy of collisional evolution are given for several cases in Figures 4 - 6. The case illustrated

TABLE 1

Density (g/cm^3): 5.0

Impact Strength (erg/cm^3): 1.5×10^8

Size Range (km): 0.8 → 250

Fraction of Collisional KE into Ejecta KE: 0.1

Slope of Ejecta Velocity Distribution: 2.25

Mass Excavation Coefficient for Cratering Impacts: 1×10^{-9}

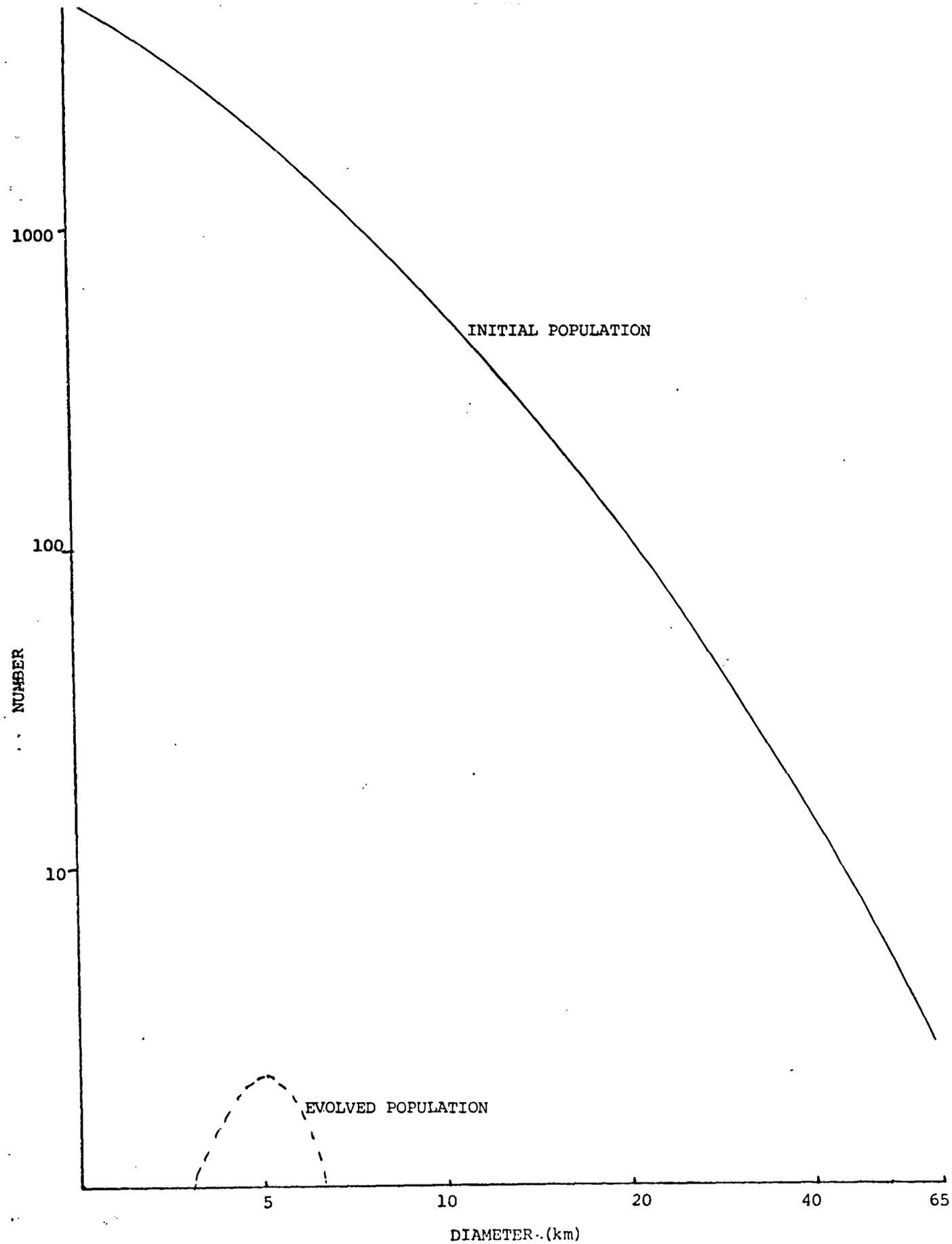

FIGURE 4: COLLISIONAL EVOLUTION OVER 1.4×10^8 YEARS AT $\underline{a}$ = 0.20 A.U., WITH AN APPROXIMATE POWER LAW INITIAL DISTRIBUTION. OVER THE AGE OF THE SOLAR SYSTEM, NEARLY COMPLETE COLLISIONAL DESTRUCTION WOULD RESULT.

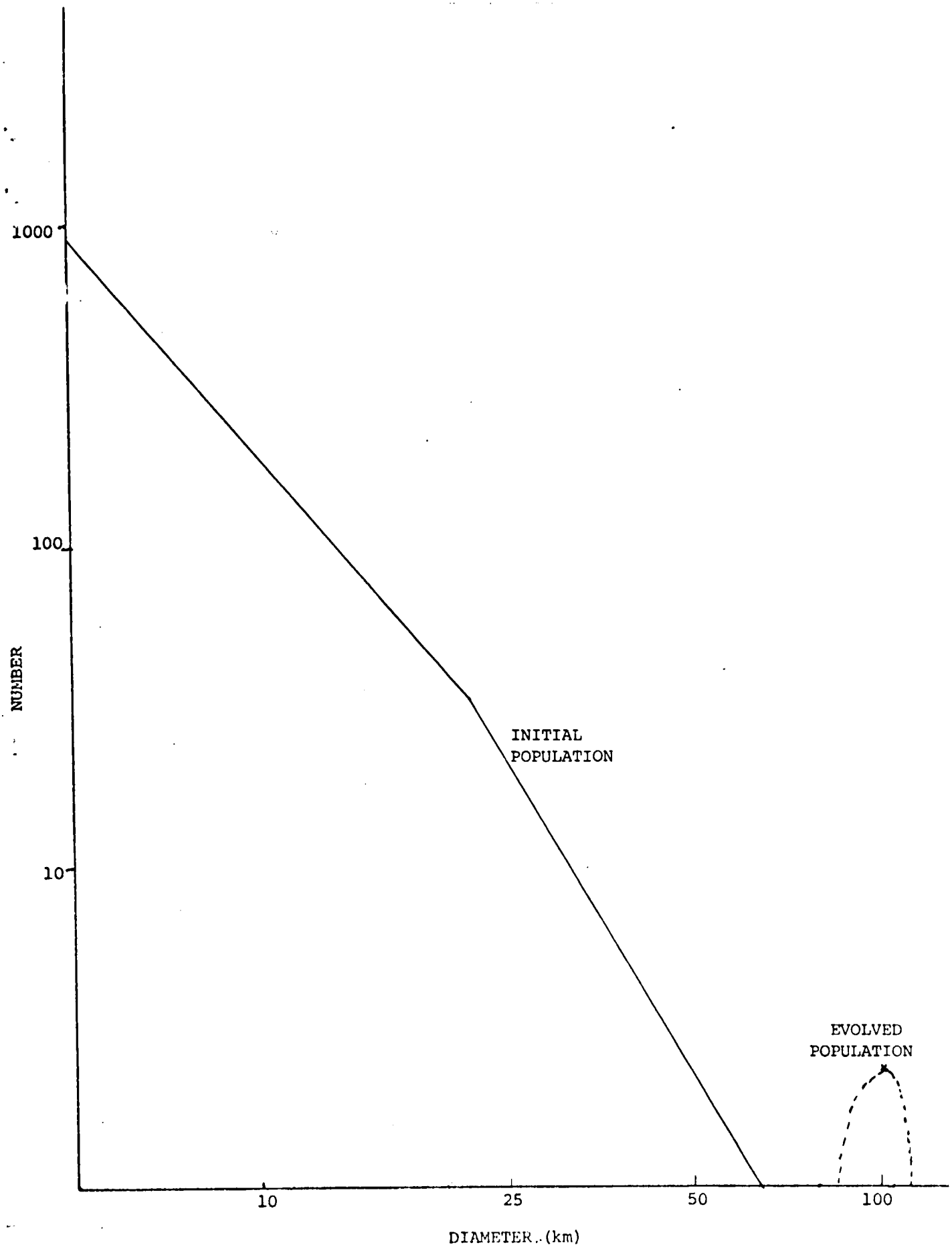

FIGURE 5. COLLISIONAL EVOLUTION OVER THE AGE OF THE SOLAR SYSTEM AT $\underline{a}$ = 0.15 A.U. THE INITIAL POPULATION UNDERGOES ACCRETION AT THE LARGEST SIZES AND FORMS A FEW LARGE BODIES WITH MOST OF THE INITIAL MASS: THE REMAINDER IS GROUND DOWN TO SMALL SIZES AND REMOVED BY RADIATION EFFECTS.

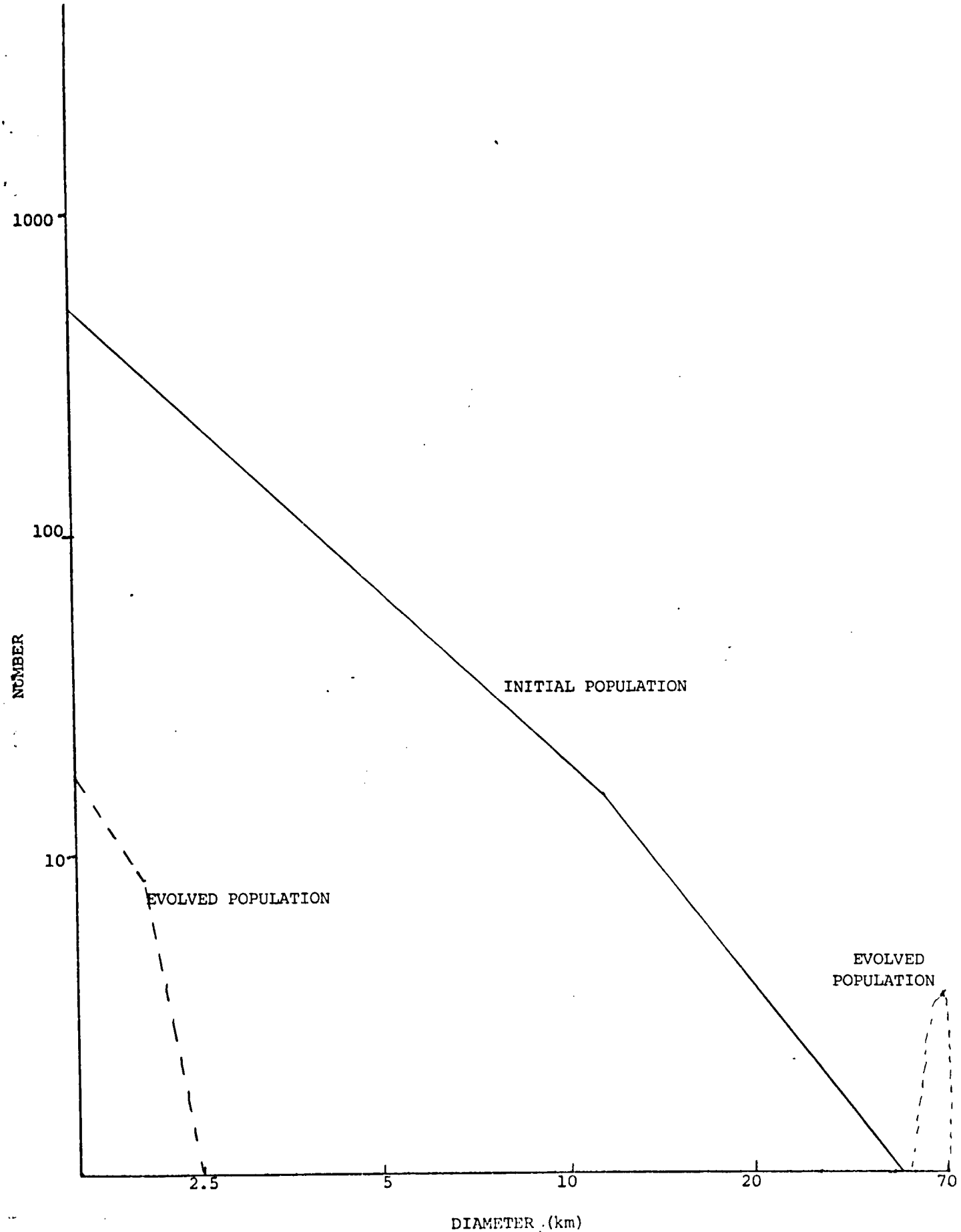

FIGURE 6. COLLISIONAL EVOLUTION FOR 5 x 10^7 YEARS AT $\underline{a}$ = 0.15 A.U. THE INITIAL POPULATION HERE IS SMALLER THAN THAT OF FIGURE 5.

in Figure 4 of a zone centered at $\underline{a}$ = 0.20 A.U. indicates that substantial collisional destruction takes place, and that over the age of the solar system, collision speeds are high enough in this region that bodies initially smaller than ∿75 - 100 km would be collisionally destroyed. However, at smaller heliocentric distances where collision speeds are lower, the collisional models suggest that particles could survive over the age of the solar system. As seen in Figures 5 and 6, at $\underline{a}$ = 0.15 A.U., the initial population undergoes accretion at the largest sizes and collisional erosion and destruction at smaller sizes. The numerical outcomes show that there could be large bodies ∿100 km diameter existing in regions interior to $\underline{a}$ = 0.15 A.U. At even smaller semimajor axes where mean collision speeds are lower, less collisional destruction would be expected and more bodies would likely survive.

Our results concerning the fate of planetesimals that were initially located within Mercury's orbit are summarized in Figure 7. The region interior to Mercury's orbit ($a < 0.30$ A.U.) divides into 4 zones: (i) for $0.25 \leq \underline{a} < 0.30$ A.U., objects are swept up by Mercury; (ii) for $\sim 0.15 \leq \underline{a} < 0.25$ A.U., bodies are destroyed by mutual collision; (iii) for ~ 0.07 A.U. $< \underline{a} < 0.15$ A.U., this is the possible survival zone for strong, iron-rich bodies; and (iv) $a \leq 0.07$ A.U. is the region in which iron bodies as large as 100 km initially would totally evaporate over the age of the solar system.

Searches for intra-Mercurial objects should be concentrated on the zone from 0.07 A.U. to 0.15 A.U. It is interesting to

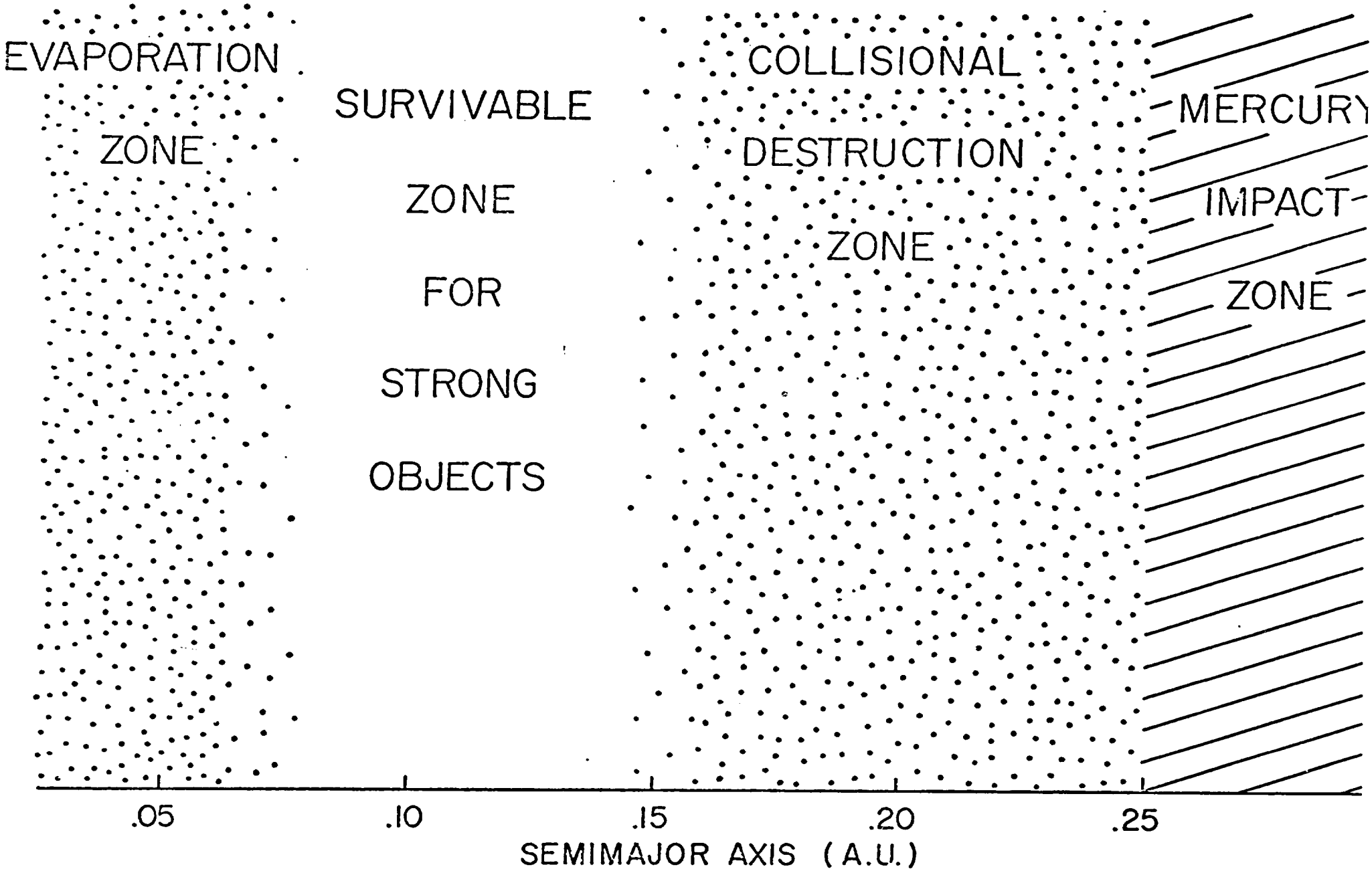

FIGURE 7. EVOLUTION OUTCOMES AT DIFFERENT SOLAR DISTANCES WITHIN MERCURY'S ORBIT.

note that eclipse photographic searches by Courten (1976) suggest the possible existence of small objects at or within a = 0.093 A.U., which is well within our stable zone. In a recent paper, Brecher et al. (1979) theoretically examine the possibility of ring around the Sun, and they estimate that a lower bound on the survivability zone is 0.02 A.U., assuming carbon bodies rather than the iron particles are used. No upper bound was calculated. In light of the growing interest in the possible existence of intra-Mercurial objects as well as the large scientific value of such objects if they do exist, it is quite important that observational searches be undertaken for objects hidden within the dazzling glare of the Sun.

REFERENCES

Brecher, K., A. Brecher, D. Morrison and I. Wasserman (1979). Nature 282, 50-52.

Campbell, W.W., and R. Trumpler (1923). Publ. Astron. Soc. Pacific 35, 214-216.

Courten, H.C., and D.W. Brown (1976). Bull.A.A.S., 8, 504.

Davis, D.R., C.R. Chapman, R. Greenberg, S.J. Weidenschilling, and A.W. Harris (1979). In Asteroids, Univ. of Arizona Press, T.G. Gehrels, ed.

Greenberg, R., J. Wacker, W.K. Hartmann and C.R. Chapman (1978). Icarus 35, 1-26.

Lebofsky, L.A. (1975). Icarus 25, 205-217.

Lewis, J.S. (1972). Earth Planet. Sci. Lett., 15, 286-290.

Perrine, C.D. (1902). Lick Obs. Bull., 1, 183.

_____ (1906). Lick Obs. Bull., 4, 115.

_____ (1909). Lick Obs. Bull., 5, 95.

Safronov, V.S. (1969). NASA TTF-667.

Weidenschilling, S.J. (1978). Icarus 35, 99-111